Wide-spread Occurrence and Increasing Trend of Biogenic Aerosol Precursors in the Arctic Ocean Simulated by an Ocean Biogeochemical Model

M. Zeising[1]*, L. Oziel[1], Ö. Gürses[1], J. Hauck[1], B. Heinold[2], S. N. Losa[1,3], S. Thoms[1], M. van Pinxteren[2], C. Völker[1], S. Zeppenfeld[2], A. Bracher[1,4]

[1]Alfred Wegener Institute Helmholtz Center for Polar and Marine Research, Bremerhaven, Germany.

[2]Leibniz Institute for Tropospheric Research, Leipzig, Germany.

[3]Shirshov Institute of Oceanology, Russian Academy of Sciences, Moscow, Russia.

[4]Institute of Environmental Physics, University of Bremen, Bremen, Germany.

Corresponding author: Moritz Zeising (moritz.zeising@awi.de)

Key Points:

- Occurrence of biogenic aerosol precursors follow phytoplankton blooms in the Arctic Ocean temporally and spatially.
- Highest values of biogenic aerosol precursors are predicted for June-August in the Fram Strait and on the Arctic shelves.
- Simulation shows a split into regions with an increasing and decreasing trend of precursors from 1990 to 2019.

Abstract

Biogenic aerosol precursors from phytoplankton production can affect cloud properties, especially in remote regions such as the Arctic Ocean. Reliable estimates on variability and trend of these precursors are required as extensive measurements in the Arctic are still scarce. We present a setup of the coupled ocean biogeochemical model FESOM2.1-REcoM3 where we integrated dissolved carboxylic acid containing polysaccharides (PCHO) and Transparent Exopolymer Particles (TEP) to describe these precursors in the upper ocean. We define PCHO as one part of the excreted organic carbon, which can then aggregate to form larger particles, TEP. Compared to observations, the simulation provides a valid TEP estimate with mean concentrations of 200-400 µg C L^{-1} on the continental shelves and 10-50 µg C L^{-1} in the central basins (0-30 m depth range). Further, the simulation for 1990-2019 reveals a significant positive trend of TEP of 0.5-3 µg C L^{-1} yr^{-1} during July-September in the Amerasian Basin (+3.5% yr^{-1}), the Canadian Archipelago (+1.2% yr^{-1}) and the Kara Sea (+0.8% yr^{-1}), in contrast to the eastern Fram Strait (-0.4% yr^{-1}), the Barents Sea (-0.3% yr^{-1}), and parts of the Eurasian Basin with a significant decrease of -0.5-2 µg C L^{-1} yr^{-1}. Our study provides for the first time an integration of TEP formation, aggregation and remineralization processes into a global ocean biogeochemical model. This simulation assembles valuable data on biogenic aerosol precursors, and as such, fills a gap on which Earth System Models can greatly benefit to improve the understanding of aerosol feedbacks within the Arctic climate.

Plain Language Summary

Aerosols are tiny particles in the atmosphere, which can affect cloud characteristics. In remote regions as the Arctic Ocean, where land or human impacts are low, local sources of aerosols are important. Small algae in the upper ocean water column can produce precursors of these aerosols, which can then be transferred into the atmosphere. Using an ocean biogeochemical model, these precursors are simulated to occur in summer in higher amounts on the Arctic shelves compared to the central Arctic Ocean basins, which agrees to observations. Furthermore, the simulated precursors exhibit two different trends: an increase in large parts of the Arctic Ocean, and a decrease in the eastern Fram Strait and Barents Sea, analyzing three decades of model output. The results of this study can be useful to simulate more explicitly the impacts of aerosols to the Arctic climate.

1 Introduction

The IPCC expects the polar region, and the Arctic Ocean in particular, to be at the forefront of climate change and profoundly altered in a future world (Pörtner et al. 2019). Those rapid changes are best illustrated by the loss of about 50% of the sea-ice volume during the last decades (Kwok 2018; Serreze & Meiers, 2019 Stroeve & Notz, 2018) and an atmospheric warming up to four times faster than the global averages (Rantenen et al., 2022), the so-called "Arctic Amplification" (Serreze & Barry, 2011). This Arctic Amplification of global warming may be caused by a combination of (positive) feedback processes (Goosse et al., 2018; Pithan & Mauritsen, 2014; Taylor et al., 2022).

Part of these feedback processes are clouds, which have a major role for the Arctic radiation budget (Goosse et al., 2018). The net cloud radiative effect depends on microphysical cloud properties such as the presence of liquid or ice phase (Shupe & Intrieri, 2004). Indeed, measurements suggest that Arctic (liquid-containing) clouds have a net overall surface warming

effect throughout the year due to the increase of downwelling longwave radiation, except for a short period in summer (Ebell et al., 2020; Intrieri, 2002). The exact trend and direction of cloud characteristics and their feedback in the Arctic in the context of climate change remains uncertain (Block et al., 2020; Pithan & Mauritsen, 2014; Vihma et al, 2016): On the one hand, the decrease of sea-ice area can lead to increase downwelling longwave radiation in polar winter months via higher low-level cloud cover (positive, i.e. self-reinforcing, feedback); on the other hand, a warmer climate can result in higher liquid content in mixed-phase clouds which leads to higher reflectivity of incoming shortwave radiation in polar summer (Goosse et al., 2018; Pithan & Mauritsen, 2014; Taylor et al., 2022).

Especially in remote marine regions, organic aerosol particles out of the upper ocean have been shown to act as cloud condensation nuclei (CCN) or ice nucleating particles (INP) (Hartmann et al., 2020; Irish et al., 2017; Leck & Bigg, 2005; Orellana et al., 2011; Wilson et al., 2015). Further, retreating sea-ice and a warming ocean might result in different temporal occurrence and new local sources of CCN and INP (Schmale et al., 2021; Taylor et al., 2022). Biogenic INP might originate from local features in the open water areas like leads in the sea-ice or ongoing melting cycles (Galgani et al., 2016; Hartmann et al., 2020; Irish et al., 2017; Zeppenfeld et al., 2019). Especially biological active parts of the marginal ice zone and aged melt ponds have been found to contain efficient ice-nucleating substances. Aerosol particles in the Arctic may contain, among many other organic compounds, polysaccharides and proteinaceous material; both two chemical groups are known for their ice nucleating activity (Hawkins & Russell, 2010; Irish et al., 2017; Wilson at el., 2015).

Dissolved polysaccharides are combined carbohydrates and belong to the Dissolved Organic Carbon (DOC) pool, which includes carbohydrate, lipid and proteinaceous compounds (Ogawa & Tanoue, 2003). In general, polysaccharides form the major part of the carbohydrate pool in the ocean (Ogawa & Tanoue, 2003; Pakulski & Benner, 1994) and are often carboxylic acid containing (Krembs & Deming, 2008). Phytoplankton produce polysaccharides as anti-freezing agents (Krembs & Deming, 2008), against salinity stress (Steele et al., 2014) or under nutrient stress, when polysaccharides are actively exudated, a process which is referred to as carbon-overconsumption or carbon-overflow (Engel et al., 2004; Engel et al., 2020). Dissolved carboxylic acid containing polysaccharides (PCHO) are defined as dissolved filtered precursors (< 0.2 microns) of Transparent Exopolymer Particles (TEP) and can contribute to the carbon transfer from the dissolved to the particulate organic carbon pool via aggregation of PCHO with other PCHO molecules and aggregation of PCHO with TEP (Alldredge and Crocker, 1995; Passow, 2002). TEP are defined methodologically as particles stainable by Alcian Blue (Alldredge et al., 1993; Engel, 2009; Passow, 2002). From the ocean surface, TEP can be transferred to the atmosphere due to breaking waves and form organic aerosol particles (or sea-spray aerosol particles). Recently, high TEP number concentrations and high TEP mass concentrations were reported in ambient marine aerosol particles, suggesting that gel-like particles can also directly constitute more than half of the particulate organic matter mass (Aller et al., 2017; van Pinxteren et al., 2022). Additionally, TEP have been shown to be a good tracer for other biogenic aerosol formation processes (Park et al., 2019). In this study, we decided to focus on PCHO and TEP formation, because they represent the tracers for biogenic INP that are crucial for cloud formation.

Indeed, considering TEP production in Earth System models are expected to greatly improve the representation of clouds and of the Arctic Amplification and the climate projection

capacities. However, to the best of our knowledge, TEP formation, aggregation and also remineralization have not been integrated into global ocean biogeochemical models, which also constitute important components of Earth System Models. Cloud formation parametrizations in Earth System Models remain simplistic and do not yet allow to investigate possible feedbacks (Block et al., 2020; Pithan & Mauritsen, 2014).

Here, we here aim to fill this gap by integrating, testing and analyzing a TEP parametrization into a "state-of-the-art" ocean biogeochemistry model. We make use of a TEP aggregation model developed by Engel et al. (2004) that was integrated into the third version of the Regulated Ecosystem Model (REcoM3, Gürses et al. 2023). In this study, we focus on the understanding of the seasonal dynamics of TEP production and regional trends in the Arctic Ocean. Because TEP is produced from PCHO during primary production, we firstly assess the performance of this new parametrization by investigating the phytoplankton chlorophyll distribution in the entire Arctic Ocean and examining the bloom phenology in Fram Strait, as an example and data-rich region Then, we present the occurrence patterns and decadal trends of TEP throughout the Arctic Ocean and put them into perspective of the global ocean.

2 Materials and Methods

We first introduce the specific ocean biogeochemical model FESOM-REcoM used (section 2.1), before detailing the model implementation of DOC, PCHO and TEP (section 2.2), the specifications of the model simulation (section 2.3), the processing of model results (section 2.4), and presenting the evaluation data sets from remote sensing and *in situ* measurements (section 2.5).

2.1 Ocean circulation and biogeochemical model

We used the coupled setup of the biogeochemical Regulated Ecosystem Model version 3 (REcoM3) and the general circulation and sea-ice Finite VolumE Sea-ice Ocean Model version 2.1 (FESOM2.1). FESOM is an unstructured-mesh ocean circulation model which allows high spatial resolution in dynamically active regions, while including the remainder of the global ocean at a coarse resolution (Wang et al., 2014). FESOM applies a finite-volume discretization instead of finite-elements previously used, optimizing computational costs and enabling a straight-forward flux definition (Danilov et al., 2017; Koldunov et al., 2019).

REcoM3 represents the ocean biogeochemistry and ecosystem, and describes the carbon cycle, nutrients (N, Si, Fe), two phytoplankton functional types (namely diatoms and nanophytoplankton), two zooplankton types (small zooplankton, polar macrozooplankton), dissolved as well as particulate organic matter, and detritus. Gravitational sinking of particles through the water column is simulated with depth-dependent sinking speed, and accumulation in the benthos is represented by one benthic layer. The model allows for variable phytoplankton stoichiometry (Hauck et al., 2013; Schourup-Kristensen et al., 2014). A first version of REcoM was presented in Schartau et al. (2007), a second version (REcoM2) was developed by Hauck et al. (2013) and Schourup-Kristensen et al. (2014), while REcoM3 was extended to include two zooplankton and detritus classes developed by Karakuş et al. (2021). Gürses et al. (2023) present a detailed description and assessment of the REcoM3 performance on the global scale. As a result of model development to REcoM2 and 3, the organic carbon pools were adapted to take into account the two phytoplankton, two zooplankton, and two detritus classes. For this study, we specified the cycle of organic carbon through the dissolved, particular and intracellular carbon

pools by adding the process description for dissolved carboxylic acidic containing polysaccharides (PCHO) and Transparent Exopolymer Particles (TEP), following Engel et al. (2004) and Schartau et al. (2007). REcoM3 now includes 30 different biogeochemical tracers (c.f. Tab. A1 in Gürses et al., 2023).

2.2 Model implementation of dissolved organic carbon, polysaccharides and transparent exopolymer particles

Engel et al. (2004) and Schartau et al. (2007) developed generalized equations and parametrization for the excretion and aggregation of organic carbon particles. The quantitative description of these processes was obtained by a mesocosm experiment of Engel et al. (2004) and consecutively integrated in the first version of the Regulated Ecosystem Model (Schartau et al., 2007). The PCHO and TEP pool were omitted in recent model releases but re-integrated in this study. In a first step, organic carbon is exudated by phytoplankton as two different dissolved, labile compounds: as PCHO and as residual DOC (considered consisting of labile organic compounds, but the chemical composition is not specified in greater detail). In a second step, multiple PCHO molecules may form aggregates, or adhere to already existing TEP particles.

DOC sources are now represented with excretion of intracellular carbon by both phytoplankton and both zooplankton classes, and detrital carbon degradation of both detritus classes. The remineralization to Dissolved Inorganic Carbon (DIC) is the only sink for DOC. The simulated source minus sinks term results as follows (see list of variables, parameters below):

$$
\begin{aligned}
S(DOC) = & \underbrace{(1 - f_{PCHO}) \cdot \varepsilon^{C}_{phy} \cdot f^{lim}_{phy} \cdot C_{phy}}_{\text{excretion by small phytoplankton}} + \underbrace{(1 - f_{PCHO}) \cdot \varepsilon^{C}_{dia} \cdot f^{lim}_{dia} \cdot C_{dia}}_{\text{excretion by diatoms}} \\
& + \underbrace{\varepsilon^{C}_{zoo1} \cdot C_{zoo1}}_{\text{excretion by zooplankton}} + \underbrace{\varepsilon^{C}_{zoo2} \cdot C_{zoo2}}_{\text{excretion by macrozoo.}} + \underbrace{\rho_{POC} \cdot f_T \cdot C_{det1} + \rho_{POC} \cdot f_T \cdot C_{det2}}_{\text{remineralization of detritus}} \\
& - \underbrace{\rho_{DOC} \cdot f_T \cdot C_{DOC}}_{\text{remineralization to DIC}}
\end{aligned}
\tag{1}
$$

The limiter functions f^{lim}_{phy} and f^{lim}_{dia} regulate the phytoplankton metabolic processes via a non-linear function based on the intracellular nitrogen to carbon ratios (N:C ratio) following Geider et al. (1998) and modified for REcoM in Schourup-Kristensen et al. (2014). The limiter function is zero for N:C ratios above the set value of N:C = 21.2:106 = 0.2. No nitrogen uptake and no carbon excretion take place. When the N:C ratio becomes lower, the limiter function increases, hence, both nitrogen uptake and carbon excretion of phytoplankton start. When the current N:C ratio is lower than the Redfield ratio (N:C = 16:106 = 0.151), the limiter function is one, not limiting uptake nor excretion (c.f. Section A3.6 in Gürses et al, 2023; Section A6.1 in Schourup-Kristensen et al., 2014).

We implemented the source and sink terms for PCHO and TEP into the current REcoM version 3 as follows: A fraction of the excreted organic carbon by small phytoplankton and diatoms builds up the PCHO pool, the aggregation of PCHO with other PCHO or with already existing TEP decrease the PCHO pool. These aggregation processes are described as cluster-cluster aggregation via Smoluchowski equations (Engel et al., 2004 and references therein) and depend on the concentration of PCHO and TEP, on the stickiness of the substrates, and on the collision kernels specific for PCHO-PCHO and PCHO-TEP interaction (c.f. Box 1 in Engel et

al., 2004). The collision kernels describe the probability of encounter of molecules. The TEP pool is increased by aggregation products of PCHO-PCHO and PCHO-TEP and diminished by remineralization to DIC.

$$\begin{aligned} S(PCHO) = \quad & \underbrace{f_{PCHO} \cdot \varepsilon^{C}_{phy} \cdot f^{lim}_{phy} \cdot C_{phy}}_{\text{excretion by small phytoplankton}} + \underbrace{f_{PCHO} \cdot \varepsilon^{C}_{dia} \cdot f^{lim}_{dia} \cdot C_{dia}}_{\text{excretion by diatoms}} \\ & - \underbrace{\alpha_{PCHO} \cdot \beta_{PCHO} \cdot C_{PCHO} \cdot C_{PCHO}}_{\text{aggregation of PCHO with PCHO}} \\ & - \underbrace{\alpha_{TEP} \cdot \beta_{TEP} \cdot C_{PCHO} \cdot C_{TEP}}_{\text{aggregation of PCHO with TEP}} \end{aligned} \tag{2}$$

$$\begin{aligned} S(TEP) = \quad & \underbrace{\alpha_{PCHO} \cdot \beta_{PCHO} \cdot C_{PCHO} \cdot C_{PCHO}}_{\text{aggregation of PCHO with PCHO}} \\ & \underbrace{+\alpha_{TEP} \cdot \beta_{TEP} \cdot C_{PCHO} \cdot C_{TEP}}_{\text{aggregation of PCHO with TEP}} \\ & - \underbrace{\rho_{TEP} \cdot f_T \cdot C_{TEP}}_{\text{remineralization to DIC}} \end{aligned} \tag{3}$$

where the descriptions of state variables, parameters and functions are listed in Table 1.

Table 1. List of state variables, parameters and functions used in the model implementation of Dissolved Organic Carbon (DOC), dissolved carboxylic acid containing polysaccharides (PCHO) and Transparent Exopolymer Particles (TEP).

State variables	Description	Value	Unit
C_{phy}	carbon concentration of small phytoplankton		[mmol C m^{-3}]
C_{dia}	carbon concentration of diatoms		[mmol C m^{-3}]
C_{zoo1}	carbon concentration of zooplankton		[mmol C m^{-3}]
C_{zoo2}	carbon concentration of polar macrozooplankton		[mmol C m^{-3}]
C_{det1}	carbon concentration of detritus class 1		[mmol C m^{-3}]
C_{det2}	carbon concentration of detritus class 2		[mmol C m^{-3}]
C_{DOC}	carbon concentration of DOC		[mmol C m^{-3}]
C_{PCHO}	carbon concentration of PCHO		[mmol C m^{-3}]
C_{TEP}	carbon concentration of TEP		[mmol C m^{-3}]
N_{phy}	nitrogen concentration of small phytoplankton		[mmol N m^{-3}]
N_{dia}	nitrogen concentration of small phytoplankton		[mmol N m^{-3}]
N_{det1}	nitrogen concentration of detritus class 1		[mmol N m^{-3}]
N_{det2}	nitrogen concentration of detritus class 2		[mmol N m^{-3}]
Parameters			
f_{PCHO}	fraction of PCHO of excreted organic carbon	0.634	
α_{PCHO}	stickiness for PCHO-PCHO	0.00087	
α_{TEP}	stickiness for PCHO-TEP	0.4	
β_{PCHO}	C-based aggregation kernel for PCHO-PCHO	0.86	[m^3 mmol C^{-1} d^{-1}]
β_{TEP}	C-based aggregation kernel for PCHO-TEP	0.064	[m^3 mmol C^{-1} d^{-1}]
ε^C_{phy}	excretion rate of organic C by small phytoplankton	0.1	[d^{-1}]
ε^C_{dia}	excretion rate of organic C by diatoms	0.1	[d^{-1}]
ε^C_{zoo1}	excretion rate of organic C by zooplankton	0.15	[d^{-1}]
ε^C_{zoo2}	excretion rate of organic C by polar macrozooplankton	0.02	[d^{-1}]
ρ_{DetC}	remineralization constant of detritus	0.15	[d^{-1}]
ρ_{DOC}	remineralization constant of DOC	0.1	[d^{-1}]
ρ_{TEP}	remineralization constant of TEP	0.1	[d^{-1}]
ϕ_{PP}	N-based maximum aggregation loss parameter for plankton	0.015	[m^3 mmol N^{-1} d^{-1}]
ϕ_{PD}	N-based maximum aggregation loss parameter for detritus	0.165	[m^3 mmol N^{-1} d^{-1}]
k_{TEP}	half-saturation const. of TEP controlled particle stickiness for aggregation of phytoplankton cells	45.0	[mmol C m^{-3}]
Functions			
f^{lim}_{phy}	limiter function for the small phytoplankton carbon excretion rate		
f^{lim}_{dia}	limiter function for the diatom carbon excretion rate		
f_T	temperature-depending Arrhenius function		

The aggregation of particles determines the amount of diatom and small phytoplankton carbon, nitrogen, and silicate transferred to the corresponding detritus pools. The aggregation rate g was calculated based on REcoM2 (see eq. 16 in SI to Hauck et al., 2013) combined with a coagulation kernel, which describes the particle stickiness depending on TEP concentration (see

eq. B13 in Schartau et al., 2007). High TEP concentrations (C_{TEP}) increase the particle stickiness and, thus, the aggregation rate g.

$$g = (\phi_{PP} \cdot N_{phy} + \phi_{PP} \cdot N_{dia} + \phi_{PD} \cdot N_{det1} + \phi_{PD} \cdot N_{det2}) \cdot \frac{C_{TEP}}{k_{TEP}+C_{TEP}} \quad (4)$$

where state variables and parameters are described in Table 1.

2.3 Specific model setup and simulation

For this study, we run FESOM2.1-REcoM3 with 4.5 km resolution in the Arctic Ocean (north of 60°N), with the so-called fARC mesh (https://gitlab.awi.de/fesom/farc) (Wang et al., 2018, Wekerle et al., 2017; Schourup-Kristensen et al., 2018). After the evaluation of the model skills to represent primary production dynamics, we turned off the photo-damage parametrization (Alvarez et al., 2019) and turned on the aeolian and riverine nitrogen input, and benthic denitrification included in REcoM3. We follow the parametrization of model processes as presented in Gürses et al. (2023). We started the ocean simulation from initial temperature and salinity fields from the Polar Science Center Hydrographic Climatology (Steele et al., 2001) and the biogeochemical simulation from initial fields of Dissolved Inorganic Nitrogen (DIN) and Dissolved Silic Acid (DSi) concentration from the World Ocean Atlas climatology (Garcia et al., 2019a, 2019b), and Dissolved Inorganic Carbon (DIC) as well as alkalinity from Global Ocean Data Analysis Project (GLODAP) version 2 (Lauvset et al., 2016). Riverine inputs of inorganic and organic carbon and nitrogen are derived from Terhaar et al. (2021).

Simulations were carried out for the period 1958-2019, i.e., a total of 61 years, with atmospheric forcing from the atmospheric reanalysis data sets of JRA55-do v.1.4.0 (Tsujino et al., 2018). We considered the period 1958-1990 as spin-up, which allows the biological processes in the surface ocean to reach quasi-equilibrium. The period of 1990-2019 was analyzed. We obtained monthly output for all years, and in addition daily output for April to September of 2017 for comparison to *in situ* observations from the ship-based "Physical feedbacks of Arctic Boundary Layer Sea ice, Cloud And Aerosol (PASCAL)" campaign PS106 on RV Polarstern. A campaign overview is presented in Macke & Flores, 2018 and Wendisch et al., 2019.

2.4 Data processing

We calculated the volume-weighted mean concentration $\bar{c}_{vw}$ for each grid cell over the depth range as:

$$\bar{c}_{vw} = \frac{\sum_i A * d_i * c_i}{V_{tot}}$$

$$V_{tot} = A * \sum_i d_i = A * d$$

with area A, thickness d_i of layer with index i, and concentration c_i corresponding to that layer.

An overall spatial mean and 0.25, 0.5, and 0.75 quantile concentrations were computed using these monthly volume-weighted mean data. A standard deviation was calculated from the volume-weighted mean over the monthly time steps. Trends were computed as linear least-square regressions based on data averaged for the months April-June and July-September over

the period 1990-2019. For regional trends, these were computed based on the corresponding regional mean and their percentaged increases were predicted from the linear regression results comparing the years 1990 to 2019. For comparison to observational data sets, we calculated a volume-weighted mean concentration of simulated TEP concentration over the same depth range as stated for observational data sets. The standard deviation was calculated over the grid points inside the area of concern and over the specific month corresponding to the observation data used.

Analysis was carried out for the Arctic Ocean and put into global perspective. Boundaries for the Arctic Ocean Basins and Seas (Fig. 1) were set according to Nöthig et al. (2020) and Randelhoff et al. (2020). As Supplementary Information, we calculated volume-weighted mean TEP and PCHO concentrations binned for Longhurst provinces (Longhurst, 2006).

2.5 Remote-sensing and *in situ* data sets for model validation

For validation of our simulation, we used the Arctic Copernicus Marine Environment Monitoring Service level 4 monthly reprocessed Ocean Color product (Product ID: OCEANCOLOUR_ARC_BGC_L4_MY_009_124) with resolution of 4 km for Total Chlorophyll *a* (TChla) – CMEMS, in the following – (Copernicus Marine Service & PML, 2022). Matching the last two decades of our simulation, CMEMS data of 2000-2019 was downloaded and processed by averaging to a summer mean concentration for TChla and its error for the months May-September. Both CMEMS and FESOM-REcoM data were interpolated to a regular grid of 0.2 degrees for comparison. As Supplementary Information, we used the Arctic Ocean Total Chlorophyll *a* product based on "AOreg.emp" from Lewis et al. (2020), constituting of the years 2003-2019, of which the Modis/Aqua TChla only was processed.

The simulated PCHO represents the dissolved carboxylic acid containing carbohydrates, which are reported to form the major part of dissolved carbohydrates in the ocean (Krembs & Deming, 2008), complemented by a small fraction of dissolved free carbohydrates (various monosaccharides). Since no observations on PCHO are available, we chose to compare simulated PCHO to *in situ* measured dissolved combined carbohydrates (DCCHO) concentration. These were derived from field bulk water samples collected at 1 m depth during the 2017 PASCAL campaign on RV Polarstern following the protocol of Zeppenfeld et al. (2020) using high-performance anion exchange chromatography coupled with pulsed amperometric detection (HPAEC-PAD). For the validation, field sample results were differentiated into three groups: (a) ice-free ocean, (b) MIZ (MIZ), and (c) leads/polynyas within the ice pack. For the model validation, we only considered the means and standard deviations of DCCHO concentration from each of the three groups. This data set is as available at Zeppenfeld et al. (2023).

TEP can be determined in water samples observationally by microscopy of abundances of particles [# L^{-1}] or determination of particle surface area [cm^2 L^{-1}] (Engel et al., 2020, Engel et al., 2009), or colorimetrically by staining with Alcian Blue solution resulting in Xanthan gum equivalents [µg Xeq L^{-1}] (Engel et al., 2009, Alldredge et al., 1993). As these methods are not fully comparable to one another, we prioritized colorimetric determined TEP. Data on *in situ* TEP concentration were converted to [µg C L^{-1}], as REcoM biogeochemical processes were described in units of carbon (TEP-C). Namely, we used data sets of Engel et al. (2020), von Jackowski et al. (2020), Yamada et al. (2015), and Wurl et al. (2011). Further, TEP concentration

of Yamada et al. (2015) were converted from Xanthan gum equivalents [µg Xeq L^{-1}] to carbon [µg C L^{-1}] by a factor of 0.05*12.01 following Engel et al. (2020).

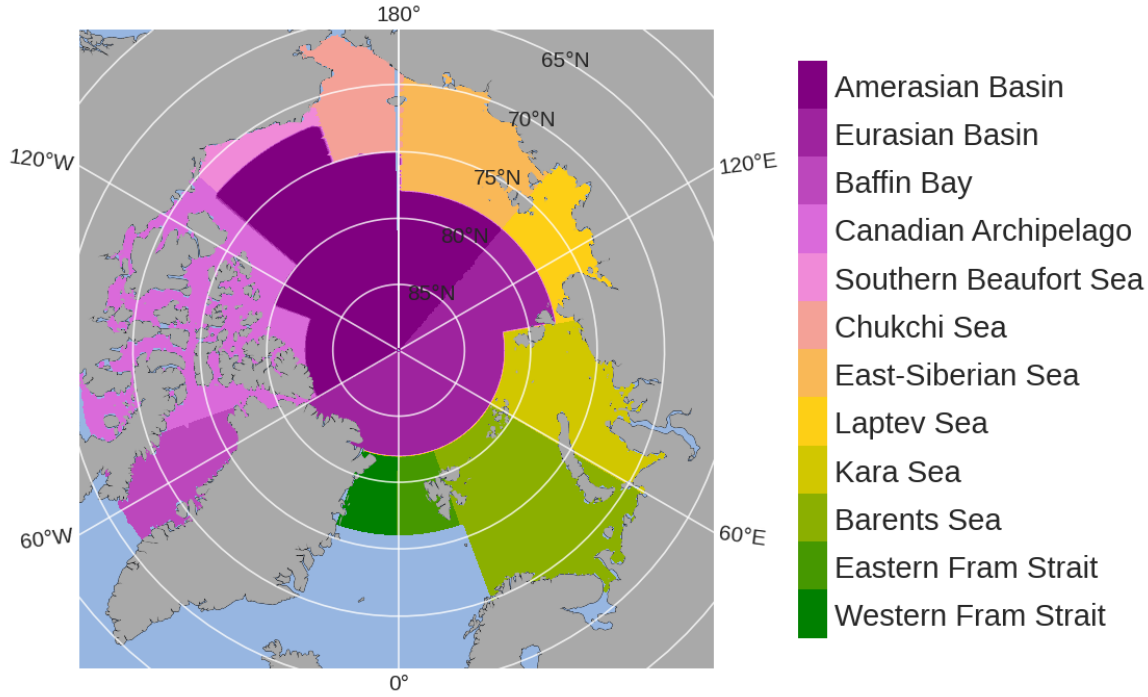

Figure 1. Map of Arctic Ocean basins and seas for evaluation of biogeochemical properties in this study, based on Nöthig et al. (2020) and Randelhoff et al. (2020).

3 Results and Discussion

Within this study, we simulate tracers for biogenic aerosol precursors by implementing the formation and degradation processes of PCHO and TEP into FESOM2-REcoM3 (Gürses et al., 2023). While this is a global model, its specific setup can be optimized in its parametrizations for the Arctic Ocean, for which already in previous setups, the Arctic biogeochemistry was simulated successfully with regard to primary production, light and nutrient availability (Oziel et al., 2022; Schourup-Kristensen et al., 2021; Schourup-Kristensen et al., 2018). In the following we present for the Arctic Ocean our new setup's predictions of phytoplankton distribution in terms of TChla and Particulate Organic Carbon (POC) concentrations (Section 3.1) and the link of phytoplankton phenology to the predicted PCHO (Section 3.2). Section 3.3 focuses on its link to TEP and Section 3.4 on the derived regional trends over the last three decades. Finally, we discuss in Section 3.5 the perspectives of the new developed FESOM-REcoM setup for global applications. In all sections FESOM-REcoM predictions are evaluated by comparisons with *in situ* and remote sensing observations, and by assessment of spatial and seasonal patterns.

3.1 Phytoplankton distribution in the Arctic Ocean

The Arctic setup of FESOM-REcoM simulates the phytoplankton seasonal cycle, where phytoplankton depends on nutrient and light availability and is controlled by zooplankton

grazing, aggregation and degradation losses, which we evaluate with Arctic remote sensing and *in situ* observations.

Figure 2 shows the phytoplankton biomass in the Arctic surface ocean in terms of TChla from our FESOM-REcoM simulations and compares it to the CMEMS Arctic satellite re-analysis product as average over the years 2000-2019 (as a mean model state) for the months when also satellite data can be obtained. FESOM-REcoM predicts highest TChla of up to 6 mg m^{-3} along the Siberian coast and on other shelf seas between 0.5-3 mg m^{-3}(Fig. 2A). In the Fram Strait, TChla predictions range from 1 to 3 mg m^{-3} with highest values in its central part, while in the central basins of the Arctic Ocean, TChla is low, with values of less than 0.2 to 0.8 mg m^{-3}. The CMEMS Arctic reanalysis remote-sensing TChla product shows no coverage of the central Arctic Ocean due to the satellite sensors configuration not enabling observations at these high latitudes (Fig. 2B). In the Barents, Kara, and Laptev Sea, TChla ranges from 0.5-5 mg m^{-3}, with peaks of up to 15 mg m^{-3} close to the coastline. In the East Siberian, Chukchi, and Beaufort Sea, the concentration of TChla is lower, ranging from 0.1-1 mg m^{-3}, also with very high values close to the coast. The error of TChla provided with the CMEMS TChla product is mostly lower than 0.5 mg m^{-3}, however along the coastline, the error increases to more than 2 mg m^{-3} (Fig. 2D). The FESOM-REcoM TChla range agrees well with CMEMS TChla, except for the inner shelf areas (Fig. 2C): In the Barents, Kara, and Laptev Sea and close to the Canadian coast FESOM-REcoM is much lower (see above). Whereas in the Chukchi and Beaufort Sea and western Fram Strait, FESOM-REcoM predicts higher TChla than CMEMS. One explanation for the observed difference may be that CMEMS average values sample far less days then are simulated by FESOM-REcoM. Schourup-Kristensen et al. (2018) explain lower TChla in the simulation by full spatial and temporal coverage whereas only open-water productive regions are accessible from remote sensing measurements. Additionally, CMEMS is error-prone on large parts of the Siberian shelves, most likely due to the very high colored dissolved organic matter and total suspended matter concentrations not accounted for in the retrieval and resulting in a strong overestimation of TChla (Heim et al., 2014; Schourup-Kristensen et al., 2018). Also, our model results show realistically the high DOC values along the coasts (data not shown). In the Chukchi and Beaufort Sea, the simulated TChla concentration itself (and the difference of FESOM-REcoM to CMEMS) is low in total values (less than 1.5 mg m^{-3}). Other observations from *in situ* observation data and other satellite-derived products draw a diverse picture in these seas with massive under-ice blooms in the Chukchi Sea with high TChla values of up to 30 mg m^{-3} (Arrigo et al. 2014), and low (0.02-0.25 mg m^{-3}) TChla concentration in the northern Chukchi and Beaufort Sea (Jung et al., 2022; Park et al. 2019).

Comparing FESOM-REcoM to the Arctic TChla product presented in Lewis et al. (2020), the range of agreement is similar as to the CMEMS product, but the spatial patterns are very different (Fig. S1 in Supplementary): This satellite product shows even lower TChla concentration in large parts of the Arctic, but agrees better to our predictions in the southern Barents Sea and Laptev Sea shelf break where TChla is still a bit higher with reaching maximum values of 7 mg m^{-3}. The authors derive TChla estimates by differentiating retrieval parameters regionally, as developed by Lewis and Arrigo (2020). This leads to a good fit to *in situ* measurements but produces abrupt changes in TChla estimates across region boundaries. The choice of methods (CMEMS compared to Lewis et al., 2020) profoundly impacts the remote sensing products. In this study, we decided to give priority to the CMEMS Arctic TChla product as it is more consistent across the whole Arctic Ocean, despite overestimation on the inner shelves.

Since satellite products have quite large errors (25-150%) and standard deviation (Fig. S1 in Supplementary) in the Arctic Ocean, we also compared our FESOM-REcoM simulations to *in situ* observations. A valuable dataset for our model evaluation is the long-term compilation of *in situ* observation data of TChla of Fram Strait and adjacent Arctic seas covering mainly the summer months May to September 1991 to 2015, presented in Nöthig et al. (2020). Following this study, we split the results of our predictions into box plots for different Arctic regions (Fig. 3), summarizing the summer months May to September of 2000-2019 (to match to the model time frame presented in Fig. 2 consistently) and evaluated for the upper 100 m depth-integrated data. TChla predictions range between 0.01-69.2 mg m^{-2} regarding 1st to 3rd quartile. Values are highest in the eastern Fram Strait with median values around 40.4 mg m^{-2}. In the western Fram Strait and in the Siberian seas, TChla median ranges from 24.5-32.9 mg m^{-2}. In the Eurasian and Amerasian Basin, median of TChla concentration is close to zero mg m^{-2} with 1st and 3rd quartile containing 0.002-14.2 mg m^{-2}. FESOM-REcoM produces some outliers with up to 350 mg m^{-2} in the eastern Fram Strait or Chukchi Sea.

Our TChla predictions compare well to the results from Nöthig et al. (2020) but also to other observations: In eastern Fram Strait, *in situ* measurements of Nöthig et al. (2020) result in integrated median values of 44 mg m^{-2} (0-100 m), and in Barents Sea of 42 mg m^{-2} which fit our model results of 40.4 and 33.8 mg m^{-2}, correspondingly (Fig. 3A). Our results are also in line with two-year round mooring observations at the long-term ecological research observatory HAUSGARTEN in the eastern Fram Strait with simulated TChla concentration reaching up to 5 mg m^{-3} in the upper 30 m compared to 7 mg m^{-3} in measurements (von Appen et al., 2021). In the marginal ice zone (MIZ), especially in the area of Fram Strait, phytoplankton growth is expected to be highest, as the sea-ice breaks up, light availability is increased and the water column is stratified (Cherkasheva et al., 2014; Nöthig et al., 2020). Likewise in the western part of Fram Strait and in the Siberian seas, the lower amount of TChla from our simulations matches *in situ* data for these regions spanning from 13-26 mg m^{-2} (Nöthig et al, 2020; Piontek et al., 2021). Integrated TChla is even lower in the Arctic Ocean basins in both simulation (median 0.01 mg m^{-2}) and measurements (7-8 mg m^{-2}). A likely explanation for the higher computed median TChla in several regions and higher variability in comparison to Nöthig et al. (2020) might be the consideration of 6-62k data points in the region subsets (Figure 1) compared to only a few hundred in Nöthig et al. (2020), where the *in situ* sampling is mostly limited to one campaign each spring-summer season. Further, our boxes span the whole Siberian seas, whereas the *in situ* measurements are located mostly in the northern parts of the shelves. Climatological maps of TChla are included as S2 in the supplements).

We assess Particulate Organic Carbon (POC) in regional boxplots similar to Nöthig et al. (2020) in Figure 3B, where POC represents the sum of the particulate carbon pools in our model, i.e., phytoplankton carbon, detrital carbon, and carbon contained in TEP. POC predictions for the 100 m depth integral range from 0.2 to18.6 g m^{-2} (1st – 3rd quartile), with highest values in the Barents Sea between 6.0-15.1 g m^{-2} and in the eastern Fram Strait with 4.7-18.6 g m^{-2}. As for TChla, intermediate values of POC (0.2-14.3 g m^{-2}) are predicted for the western Fram Strait and on the Siberian shelves. In the central Arctic basins, the amount of POC is low with 0.3 to 2.7 g m^{-2}. This is in good agreement with the observations of Nöthig et al. (2020), who measured the highest POC median of 13 g m^{-2} in the eastern Fram Strait, alongside 5-8 g m^{-2} in the western Fram Strait and on the Siberian shelves. The higher simulated values on the shelves might be caused by including also their southern parts, whereas the measurements do not cover these areas.

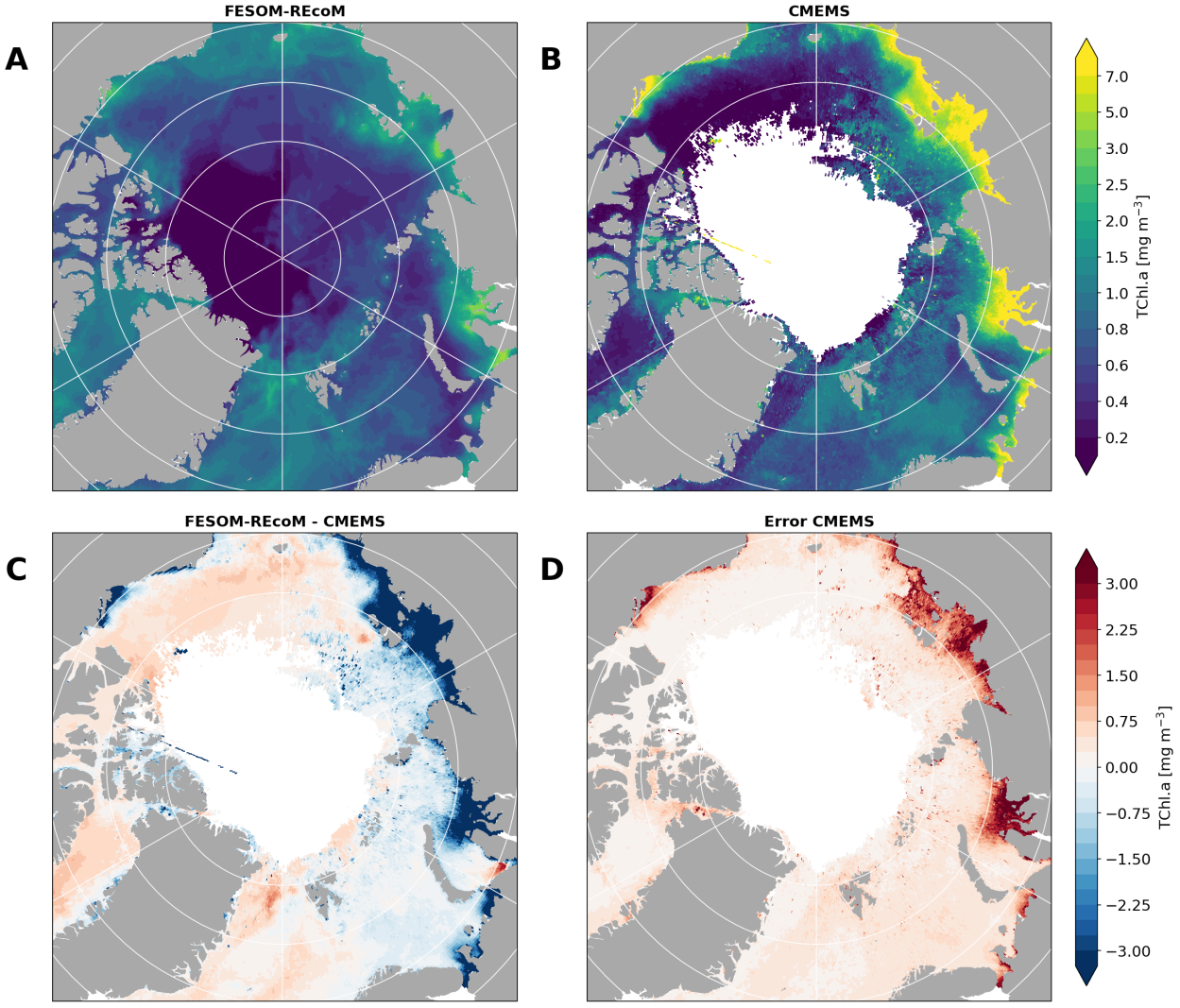

Figure 2. Maps of surface Total Chlorophyll *a* (TChla) of FESOM-REcoM (A), of the CMEMS Arctic re-analysis product (B), the difference of CMEMS to the model results (C), and the error of CMEMS (D) as average of May to September over the years 2000-2019. CMEMS data does not cover the central Arctic Ocean.

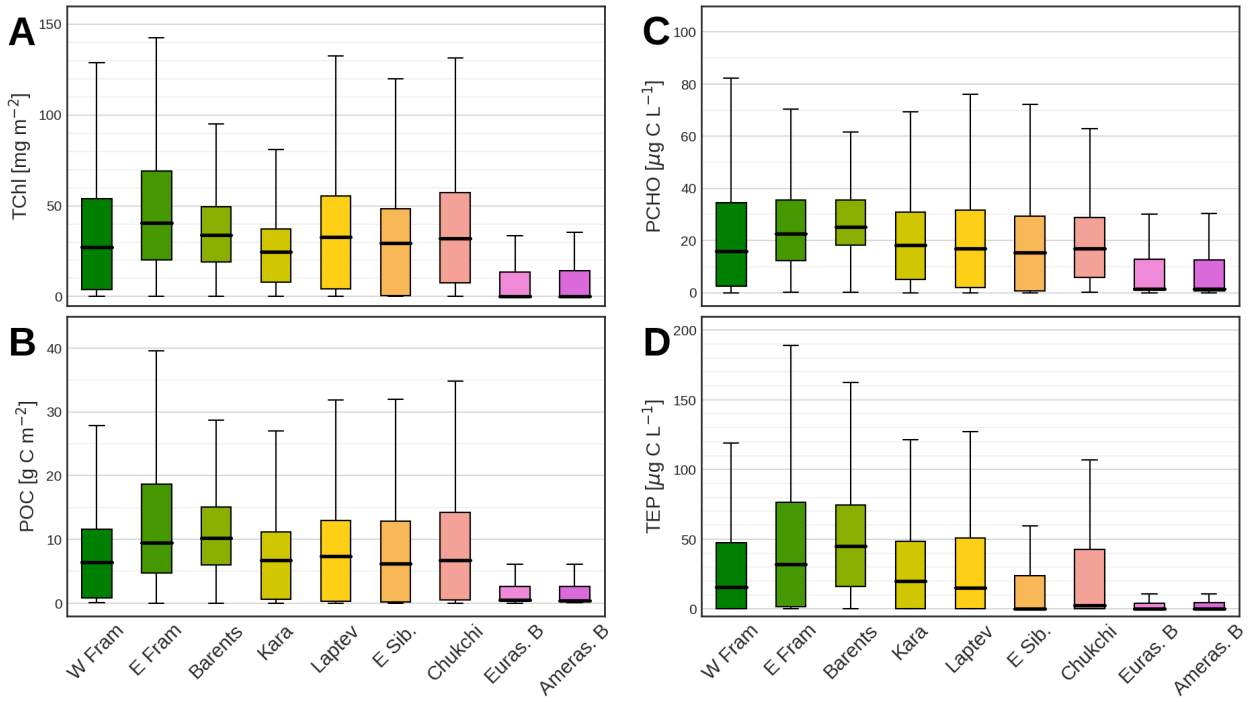

Figure 3. Box plots comparing regional differences for Total Chlorophyll *a* (TChla, A), Particulate Organic Carbon (POC, B), polysaccharides (PCHO, C), and of Transparent Exopolymer Particles (TEP, D) following the region definitions mapped in Fig. 1 for western Fram Strait (W Fram), eastern Fram Strait (E Fram), Barents Sea, Kara Sea, Laptev Sea, East Siberian Shelves (E Sib), Chukchi Sea, Eurasian Basin (Euras. B), and Amerasian Basin (Ameras. B.). Data is averaged over May to September of the 2000-2019 period, presented as depth integrated (0-100 m) values for TChla and POC and volume-weighted mean (0-100 m) for PCHO and TEP. The thick black line represents the median, the box represents the 1st and 3rd quartile. The whiskers span over 1.5 times the inter-quartile range.

3.2 Arctic PCHO distribution and its link to a phytoplankton bloom in Fram Strait

We analyze in this section the relation of the phytoplankton bloom development with the production of PCHO. Firstly, we analyze the long-term and spatially inclusive FESOM-REcoM PCHO data which are presented as 0-100 m volume-weighted mean in Figure 3C, following the presentation as done for TChla and POC. Our predictions are discussed alongside *in situ* observations. Then we focus particularly on the Fram Strait to study the time evolution of phytoplankton blooming in comparison to PCHO production in spatial context using our FESOM-REcoM predictions. We conclude with a seasonal cycle of the phytoplankton phenology to demonstrate the organic carbon flux from photosynthesis towards particle formation.

Regarding a regional overview, PCHO integrated over the upper 100 m is highest in the Barents Sea with a median of 25.3 µg C L^{-1}, while in the Siberian seas, 15.5-18.2 µg C L^{-1} are predicted. Eastern Fram Strait PCHO median concentration of 22.6 µg C L^{-1} is higher than 15.9 µg C L^{-1}in western Fram Strait (Figure 3C). For the Eurasian and Amerasian Basin, the median ranges from 1.4-1.6 µg C L^{-1}. In eastern Fram Strait, von Jackowski et al. (2020) observe DCCHO in concentrations of 55.8 µg C L^{-1} in July and 22.5 µgCL^{-1} in September (0-100 m), which are slightly higher than FESOM-REcoM summer PCHO median (Fig. 3C). Piontek et al.

(2021) report decreasing concentration with depth for the Eurasian Basin, which we also observe in our results, but to a much stronger extent. In the upper ocean, our model results fit to observations by Piontek et al. (2021) in the Eurasian Basin, the northern Barents Sea, and northern Laptev Sea, who measured 25.5-30.8 µg C L^{-1} DCCHO in the upper 40 m in August to October 2012 (compared to 10-80 µg C L^{-1} of PCHO in this study, climatological maps for 0-30 m volume-weighted mean are presented in Supplementary S3). Considering greater depths, the volume-weighted median of 0-100 m depth of PCHO in FESOM-REcoM drops to 2 µg C L^{-1}, while approx. 19-23 µg C L^{-1} DCCHO in the depth range 40-150 m are reported by Piontek et al. (2021). The authors conducted their campaign in a year of extraordinary low sea-ice concentration, which led to high TChla and a strong nutrient depletion. The high amounts of DCCHO excreted by phytoplankton were not immediately turned over by bacterial activity and could have accumulated in the water column as a result.

In order to analyze the link of phytoplankton bloom evolution and PCHO production, we chose here the time period of May to July 2017 in analogy to the 2017 PASCAL campaign and present predictions of sea-ice concentration, Dissolved Inorganic Nitrogen (DIN), TChla and PCHO of the model's surface layer (0-5 m) in Figure 4. In the northern Atlantic and Arctic Ocean phytoplankton growth predicted in our model is mostly limited by light. Early in the season, sea-ice covers most parts of the Arctic Ocean and Fram Strait. In May of 2017, the eastern Fram Strait is already ice-free (Fig. 4A). A phytoplankton bloom is formed in the northern Atlantic and in the MIZ in the Fram Strait, most prominently along the ice edge (Fig. 4G – here defined as contour of 25% SIC). This bloom shifts further north into the whole eastern Fram Strait in June, using up DIN. In the MIZ, high TChla of up to 6 mg m^{-3} is simulated. In July, SIC decreases further and TChla is predicted in the whole Fram Strait, with a major increase in the western part, and additionally in the northern Barents Sea (Fig 4C and I, respectively).

Simulated PCHO follows elevated TChla first northward and then westward in the Fram Strait area and reach surface concentration of up to 120 µg C L^{-1} (Fig. 4J, K, L), especially when DIN is depleted (Fig. 4D, E, F). In May, PCHO concentrations are most elevated close to the ice edge. In June, areas of elevated PCHO concentration are found towards the eastern Fram Strait and Barents Sea. In July, PCHO concentrations peak in the MIZ of western Fram Strait and northern Barents Sea alongside the phytoplankton blooms. Interestingly, there is a case where high TChla does not result in high PCHO concentration: in June in the South-western Fram Strait (Fig. 4K). DIN has not been used up completely in this area, hence, the phytoplankton is still not suffering from nutrient depletion. The implemented limiter function for phytoplankton carbon excretion (depending on the intracellular N:C ratio) is apparently still low, and as such, the phytoplankton cells are not excreting excessive carbon to a large extent.

In the Fram Strait area, there is also a good agreement with PASCAL campaign data of the same months of 2017, providing *in situ* measured concentrations of DCCHO in the open ocean, marginal ice zone and ice-covered regions around Svalbard, despite the simulated PCHO reflecting only a part of the DCCHO pool. Values were found to be lowest in the sea-ice leads within ice-covered regions (11.3 ± 10.1 µg C L^{-1}). A similar concentration range can be observed as well in the model results (Fig. 3). The PASCAL campaign data on DCCHO in the marginal ice zone of 51.1± 37.0 µg C L^{-1} agree as well with the model results. In the ice-free ocean, mean measured DCCHO concentration is 17.2 ± 5.2 µg C L^{-1}. In May and June of the modeled year 2017, high TChla concentrations are found in the ice-free ocean together with high DCCHO

concentration. In July, DCCHO concentration is still elevated even as TChla concentration has declined. This might be caused by increased nutrient depletion of phytoplankton and therefore, increase release of dissolved organic carbon following the carbon overconsumption hypothesis.

In order to assess the mean seasonal cycle over the years 2000-2019, phytoplankton carbon, TChla, PCHO, and TEP (the later discussed in Section 3.3) concentrations are compiled as a volume-weighted mean of the upper 30 m of the ocean for the eastern Fram Strait (Fig. 5). The twenty year climatology shows that the seasonal dynamic of TChla and PCHO follows in this region as is discussed explicitly in Figure 4 for 2017 for the surface waters. The phytoplankton carbon concentration increases to a peak of approximately 160 µg C L^{-1} in July likewise TChla, with highest concentrations of 1.5 mg L^{-1}. DIN concentration decreases from a winter average of about 4 mmol m^{-3} with the start of the phytoplankton bloom in May to 1 mmol m^{-3} in August. Following the bloom closely in time, PCHO is released by phytoplankton and its concentration rises to a maximum of approx. 25 µg C L^{-1} in July. In the following, months, PCHO concentration declines, whereas TEP concentration rises quickly from May to August to approx. 150 µg C L^{-1}, lagging approx. one month behind the phytoplankton bloom.

Overall, our PCHO prediction display that high PCHO are clearly linked to high TChla concentrations coinciding with nutrient depletion in the open ocean and in the MIZ (e.g., July 2017 in West Fram Strait, Fig. 4). Furthermore, our model results show that PCHO is not accumulated to a large extent in the upper ocean, but quickly aggregated to TEP.

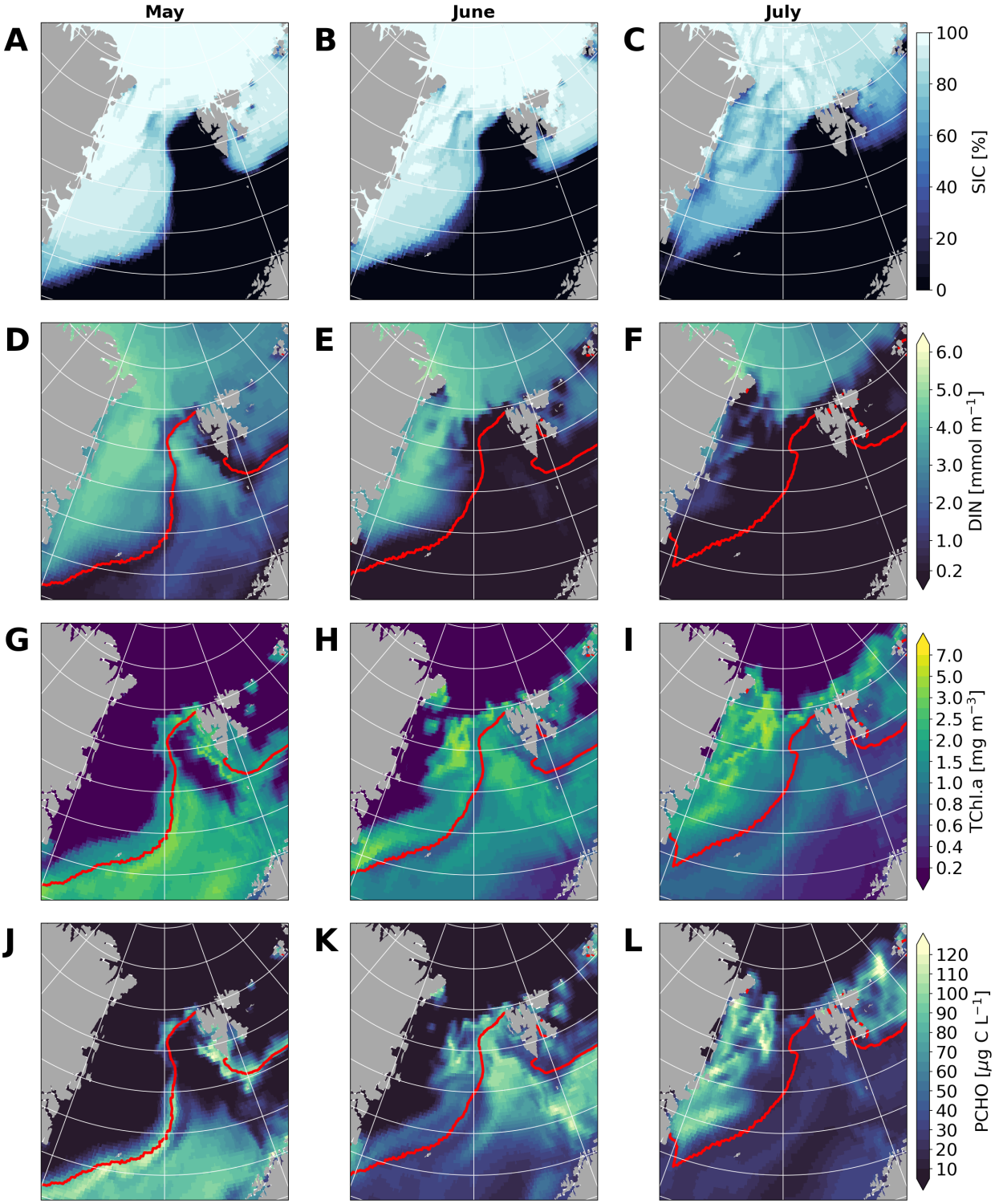

Figure 4. Maps of simulated sea-ice concentration (SIC, A-C), Dissolved Inorganic Nitrogen (DIN, D-F), Total Chlorophyll *a* (TChla, G-I) and polysaccharides (PCHO, J-L) as monthly mean of May, June, and July 2017 for the model's surface layer (0-5 m). The contour of the sea-ice edge (defined as 25% SIC) is depicted as red contour line.

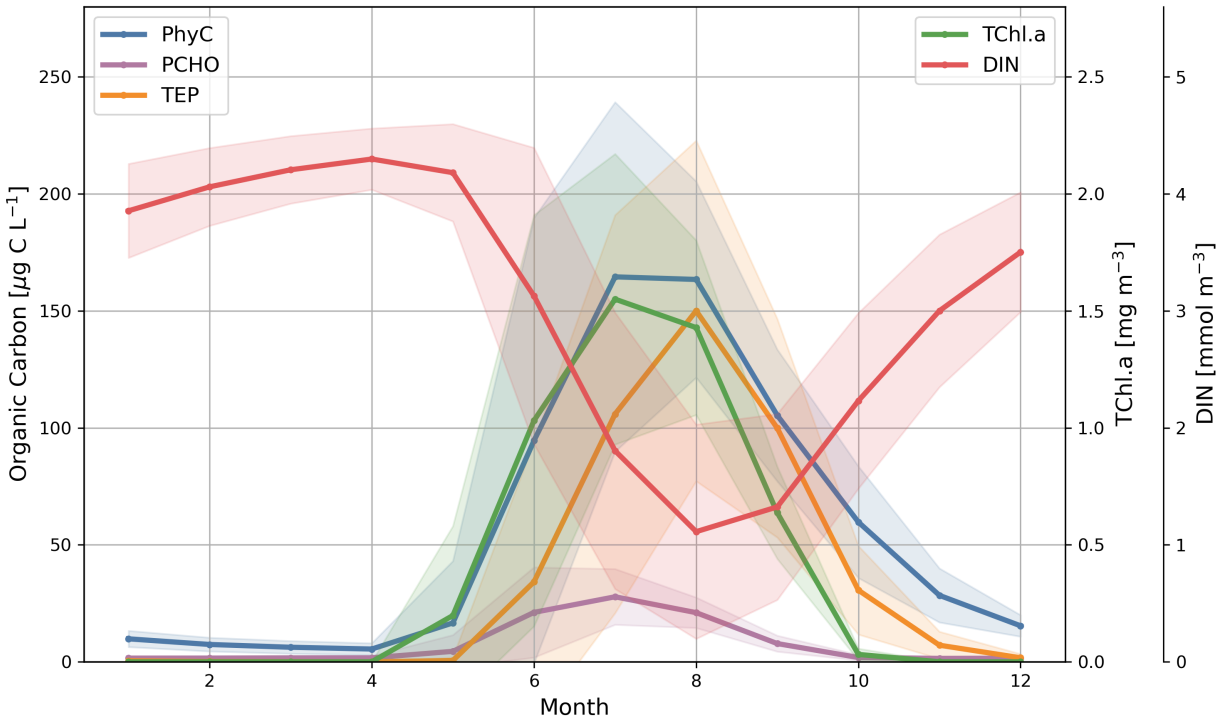

Figure 5. Seasonal cycle of simulated organic carbon of phytoplankton (blue), dissolved carboxylic acid containing polysaccharides (PCHO, purple), Transparent Exopolymer Particles (TEP, orange), on the left axis, and Total Chlorophyll *a* (TChla, green), and Dissolved Inorganic Nitrogen (DIN, red) on the right axis of the period 2000-2019 as volume-weighted mean of the upper 30 m ocean depth, averaged over the eastern Fram Strait (extent see Fig. 1). Standard deviation of the regional average is shown as shaded area in corresponding colors.

3.3 Occurrence of TEP in the Arctic

In this section we assess the prediction of TEP in the Arctic Ocean by describing its seasonal cycle in the Fram Strait, before broadening the perspective to an Arctic-wide climatology.

Following the other FESOM-REcoM variable presentations for the Fram Strait in Figure 5, also the TEP predictions exhibit a clear seasonal cycle in succession of the phytoplankton bloom (Fig. 5). In addition, Figure 5 shows that PCHO release and TEP production also depend on nutrient depletion during the bloom. This is in accordance with Engel et al. (2017) who found that TChla alone is not a good predictor for TEP in the Fram Strait. In the same region, Engel et al. (2017) also reported a strong link between TEP and phytoplankton occurrence patterns. Especially with respect to *Phaeocystis* spp., Zamanillo et al. (2019) found TEP concentration positively correlated to phytoplankton biomass along a wide transect in the Atlantic Ocean. Aggregation processes of PCHO lead to the formation of TEP, which itself further intensifies aggregation processes. According to the model formulation, the more TEP is present, the faster the aggregation process becomes.

Based on the Arctic-wide simulation, we produce monthly climatological maps of TEP for April to November and for a water depth of 0-30 m, roughly corresponding to the summer mixed layer depth in the Arctic Ocean (Peralta-Ferriz & Woodgate, 2015) (Fig. 6). In May, TEP

concentrations rise first in regions with phytoplankton blooms (c.f. monthly climatology of TChla and PCHO in Supplementary Material S2, S3), i.e., in Fram Strait and on the shelves (50-150 µg C L^{-1}). The climatology further shows that from June to August, TEP increases in the Fram Strait, on the Siberian shelves, in the Chukchi and Beaufort Sea and reaches approx. 200-400 µg C L^{-1}. TEP is also transported across the Arctic Ocean. As a result, the mean concentration in the central Arctic Ocean reaches 10-50 µg C L^{-1} in the upper 30 m of the water column. There is a gradient of TEP from the shelves towards the Arctic Ocean basins during summer in our simulation. Yamada et al. (2015) highlight this gradient in their study on the Chukchi shelf and Canadian basin (shelf 138.9±64.7 µg C L^{-1} to slope/basin: 79.3±15.5 µg C L^{-1}, 0-50 m) and attribute it to TChla co-occurrence, transport from the shelf towards the basin, and additional TEP production by prokaryotes. With the beginning of September, TEP declines in the whole Arctic realm. Then, TEP is remineralized or descends to deeper ocean layers, and surface concentrations decline. A rise in summer and quick decline in autumn is in accordance with TEP observation data sets of von Jackowski et al., 2020 (21.4 ± 14.5 µg C L^{-1} in July, 7.1 ± 5.2 µg C L^{-1}in September, 0-100 m).

Table 2 compares our model TEP results for the Artic Ocean to observations averaged to the same month and for the same depth range as provided by the *in situ* data: Considering the comparison of point observations towards monthly integrated simulations for a small area, overall, there is a good agreement, despite modeled TEP concentrations being often slightly higher and differing particularly in the region of the Catlin Ice Base. Here, Wurl et al. (2011) obtained their measurements from an under-ice phytoplankton bloom which resulted in very high production of TEP. Such an event is not reproducible by FESOM-REcoM because ice-algae are not explicitly modeled, and light-through-ice-transmission is not adequately represented.

For completeness to assess regional budgets, the TEP volume-weighted median concentrations of 0-100 m are compiled as for PCHO in Figure 3D. The highest median of 44.9 µg C L^{-1} is reached in the Barents Sea. In the eastern Fram Strait, the median lies at 31.8 µg C L^{-1}, whereas in the western Fram Strait, Kara and Laptev Sea, median concentration of 15.3-19.8 µg C L^{-1} are predicted. In the East Siberian and Chukchi Sea, as well as in the Eurasian and Amerasian Basin, median TEP concentration are below 3 µg C L^{-1}. Maxima of simulated TEP values nearly reach 190 µg C L^{-1} in the western Fram Strait.

3.4 Decadal trends in summer TEP concentration

We estimated the linear trend of TEP concentrations for the months April to June and July to September of the period 1990-2019 for the upper 30 m of the water column in the Arctic regionally (Fig. 7). Interannual regional variations of TEP are high in our simulation but have also been identified in observations. For example, in eastern Fram Strait, Engel et al. (2017) found a spread of 3-310 µg C L^{-1} for 2009-2014. To our knowledge, other long-term trends of TEP occurrence in the Arctic have not yet reported in observational studies. For early summer, TEP trends are only significant for the regions Amerasian Basin (+9.8% yr^{-1}), Canadian Archipelago (+7.4% yr^{-1}), Chukchi Sea (+3.3% yr^{-1}) as a whole (defined in Fig. 1, statistics in Tab. S4 in the Supplementary) and other, smaller areas displayed in Figure 7, of which the most prominent is a decrease located in the southern Barents Sea (-0.5-1.5 µg C L^{-1} yr^{-1}), as well as an increase in the Barents Sea opening (0.5-1.0 µg C L^{-1} yr^{-1}) and in the Kara Sea close to the Yenisey river mouth (0.5-3.0 µg C L^{-1} yr^{-1}). The area of significance of these trends is limited (hatched in Fig. 7), but we note a slight positive trend across large parts of the Arctic Ocean

(< 0.5 µg C L^{-1} yr^{-1}). Interestingly, the wide-spread positive trend in early summer manifests itself in the later summer months more prominently in the Kara Sea, the Canadian Archipelago, the Amerasian Basin (significant trend across the whole three regions with +0.8% yr^{-1}, +1.2% yr^{-1}, +3.5% yr^{-1} correspondingly), and in a significant positive trend in parts of the East Siberian, eastern Laptev, Chukchi, and Beaufort Seas (0.5-3 µg C L^{-1} yr^{-1}). Contrasting, a significant negative trend develops in the eastern Fram Strait (-0.4% yr^{-1}) and in the Barents Sea (-0.3% yr^{-1}), and in parts in the Eurasian Basin (< -0.75 µg C L^{-1} yr^{-1}). The simulated TEP trend prediction splits into two major regions: one with Atlantic water influence (Fram Strait, Barents Sea, parts of the Eurasian basin) with mainly a decrease of TEP, the other with Pacific water influence (Beaufort Sea, Chukchi Sea, parts of the Amerasian basin) exhibiting a prominent increase of TEP. Figure 5 illustrates that TEP occurrence follows phytoplankton blooms in the eastern Fram Strait with a temporal lag of approx. one month, but also depends on the nutrient limitation during blooming. In our simulation, Net Primary Production (NPP) generally increases from 1990-2019 with exception of the Barents Sea and parts of the Eurasian Basin (Fig. 7C, D), whereas nutrient availability decreases in the whole Arctic Ocean (data not shown), most strongly in the Laptev, East Siberian and Beaufort Sea. Hence in the regions of Atlantic water influence, the simulated significant decrease of NPP together with only a slight decrease of nutrient availability might result in less carbon overflow from phytoplankton production and, therefore, in the decrease of TEP concentration there. In contrast in the Laptev, East Siberian, Chukchi and Beaufort Sea, the simulated NPP increases significantly, in hand with a significant decrease of DIN, which results in the significant increase of simulated TEP concentration. NPP has been shown to increase significantly in all regions of the Arctic Ocean and seas, most strongly pronounced in the Kara, Laptev and Siberian Sea based on remote-sensing products (Lewis et al., 2020). Lewis et al. (2020) argued that the increase of NPP results from enhanced supply by nutrients. As a result of the diminishing sea-ice, light limitation is expected to decrease further in the Central Arctic Ocean, shifting the phytoplankton more towards a nutrient-limited regime (Oziel et al., 2022). Based on observations, Randelhoff et al. (2020) expect a wide-spread nitrogen limitation across the Arctic except for the central basins. In contrast, Oziel et al. (2022) predict from ocean biogeochemical modeling, that there is a nutrient limitation in the central Arctic Ocean prevailing, as DIN supply through upwelling and lateral mesoscale eddy transport does not suffice to replenish the reservoir.

Overall, we have shown that our model is capable to simulate well the TEP distributions in the Arctic Ocean. As this is a first step to simulate TEP in the Arctic Ocean, the full complexity of TEP cycling is not yet represented in the model: Other processes of the life cycle of TEP such as ballasting of TEP and consecutive sinking in the water column, or microbial/zooplankton grazing on the particles itself have not yet been implemented. Additionally, Galgani et al., (2016) describe high numbers of TEP and its precursors in melt ponds and open water of the central Arctic Ocean and argue, that TEP could also be released from melting sea-ice. Still, the peak concentration values of TEP in FESOM-REcoM, especially regarding the surface values, might be too high. A reason could be the missing transfer of particles into the sea-surface microlayer (SML) in our simulation. The SML is the very thin transition film at the ocean-atmosphere interface, which is not part of the model structure. TEP is positively buoyant, thus, the particles would ascend through the water column and get enriched in this layer (Azetsu-Scott & Passow, 2004; Wurl et al., 2011). In a methodological study, Robinson et al. (2019) demonstrate the enrichment of TEP additionally via bubble scavenging, a process when rising air bubbles transport organic matter. Observational studies report contrasting

results on SML enrichment. Galgani et al., (2016) report only minor enrichment in the surface microlayer in the open water of the Central Arctic, whereas Wurl et al. (2011) calculated an enrichment factor of 1.7±0.5 in the Canadian Arctic. One could use these enrichment factors for our simulations to retrieve an estimate of TEP concentration in the SML.

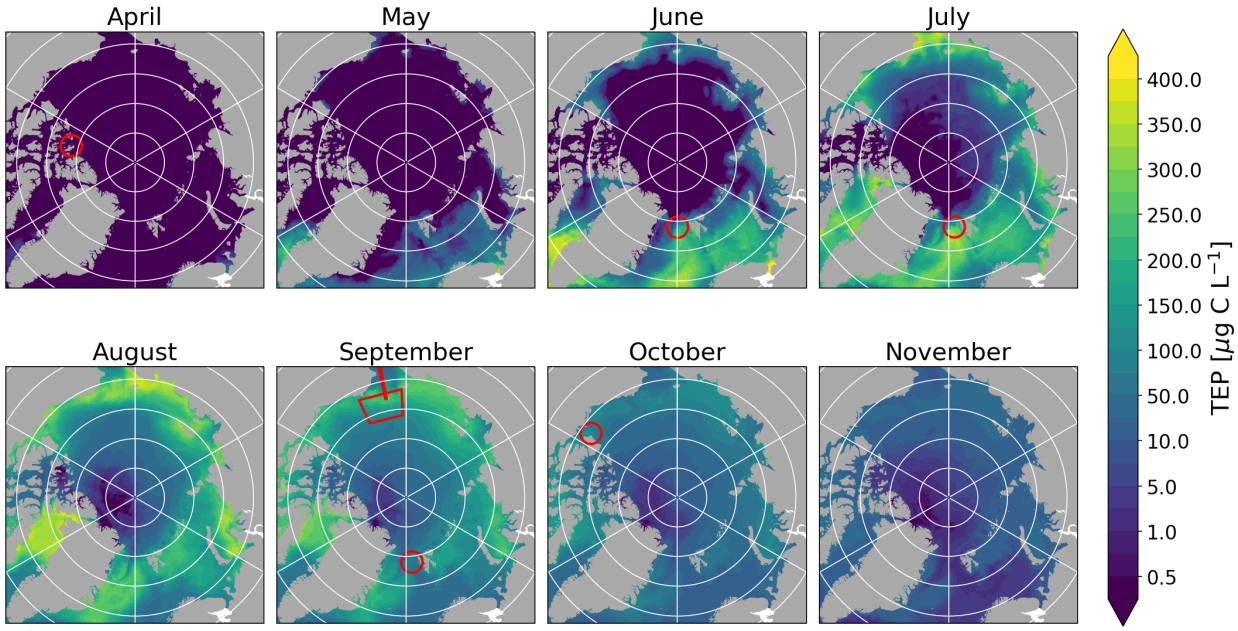

Figure 6. Climatological maps of Transparent Exopolymer Particles (TEP) concentration as volume-weighted mean of the upper 30 m of the simulated period 2000-2019. Overlayed are the positions of the observation data points in red (c.f. Tab. 2).

Table 2. Comparison of carbon concentration of TEP (TEP-C) of observational campaigns and simulation. Model results are volume-weighted and averaged corresponding to the depth range, area, and month of observations. A variable number N of model grid cells was chosen to best fit the area coverage of observations. Mean and standard deviation of the years 2000-2019 is stated in brackets.

Period	Region	Depth [m]	Modeled TEP-C [µg C L^{-1}]	Observed TEP-C [µg C L^{-1}]	Number of Samples	Reference
Mar-Apr 2010	Catlin Ice Base	0-14	0±0 (0±0)	405.9±344.7	65	Wurl et al. (2011)
Jun 2015	Fram Strait	5-200	16.0±11.3 (20.9±16.6)	8.2±6.1	935	Engel et al. (2020)
Jul 2018	Fram Strait	0-100	102.9±23.5 (88.4±35.3)	21.4±14.5	1631	von Jackowski et al. (2020)
Sep-Oct 2018	Fram Strait	0-100	32.3±7.5 (27.7±11.6)	7.1±5.2	2440	von Jackowski et al. (2020)
Sep-Oct 2012	Chukchi Shelf	0-50	115.3±72.6 (77.5±46.9)	138.9±64.7	1106	Yamada et al. (2015)
Sep-Oct 2012	Canada Basin	0-200	29.2±6.9 (23.8±11.0)	70.4±15.5	14940	Yamada et al. (2015)

Oct 2009	Northwest Passage	0-29	137.0±12.1 (108.0±33.0)	126.1±69.7	174	Wurl et al. (2011)

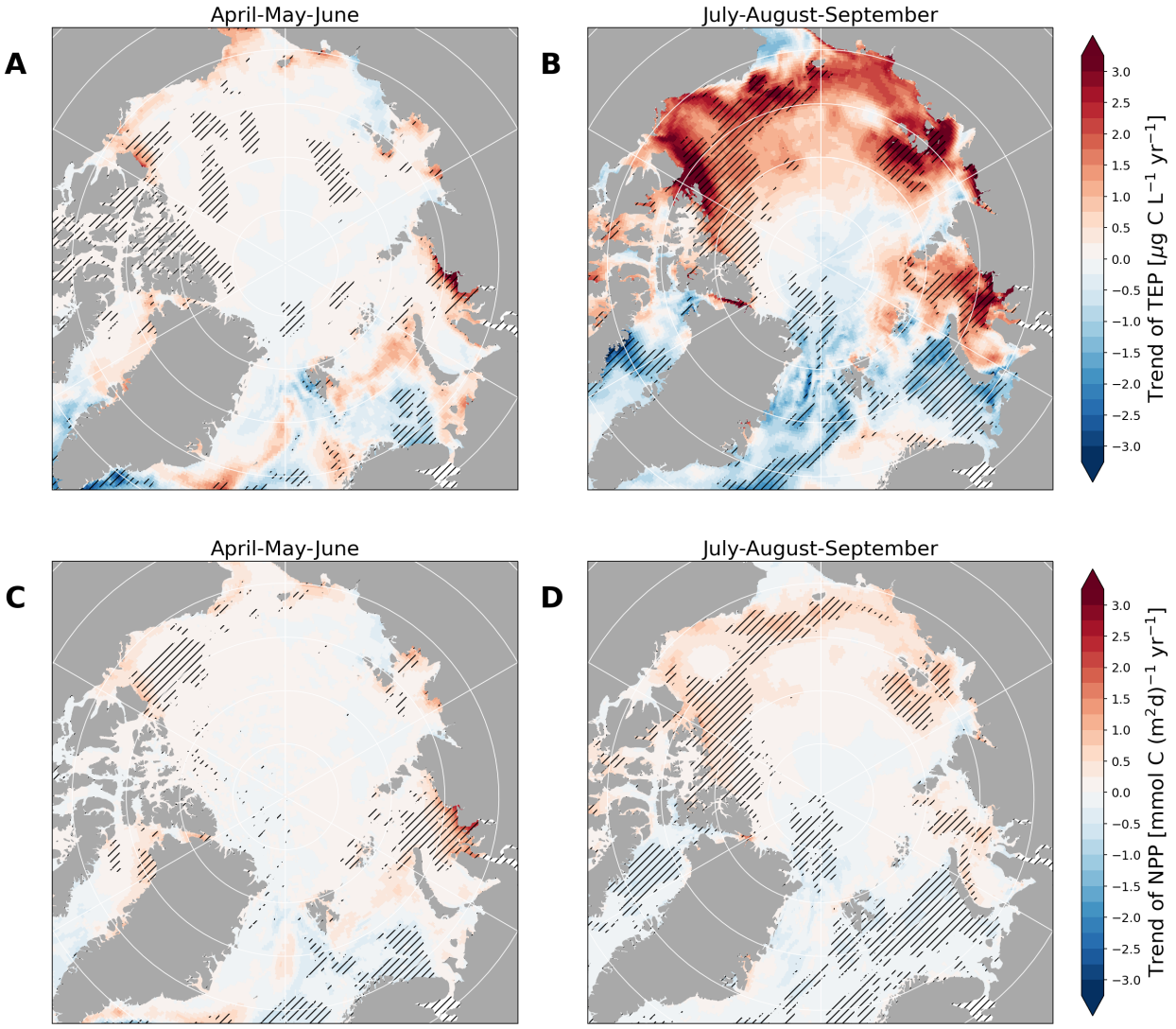

Figure 7. Maps of the trend of the volume-weighted mean TEP concentration (0-30 m) of the months April-June (A) and July-September (B) and trend of Net Primary Production (NPP) for the same months (C, D) of the simulated period 1990-2019 as volume-weighted mean of the upper 30 m. Significant trends are displayed as hatched areas.

3.5 Global TEP patterns

As detailed in section 2.3, our new FESOM-REcoM setup was optimized in its parametrization and irregular grid to enable reliable Arctic sub-mesoscale predictions of PCHO and TEP. However, since FESOM-REcoM is a global model in principle, we additionally evaluate the TEP concentration in perspective to its global pattern. Because *in situ* observations are available mostly for surface waters (see review by Wurl & Cunliffe, 2017; updated by

Zamanillo et al.; 2019), we present here the model results as volume-weighted mean of the upper 30 m of the ocean averaged over 2000 – 2019. For completeness, global model results of TChla and PCHO can be found as Supplementary Figures S5 and S6. Further, mean TEP concentrations are also summarized by binning for each Longhurst Provinces (Longhurst, 2006), presented as Table S7 in the Supplementary.

In large areas of the global ocean, simulated TEP concentration in FESOM-REcoM range from 5-50 µg C L^{-1} (Fig. 8A). TEP concentrations are especially high in the Nordic Seas and the Arctic Ocean with approx. 75-150 µg C L^{-1}. In the region of the Antarctic Polar Front and in the Peruvian upwelling, TEP concentrations reach a minimum with values below 5 µg C L^{-1}. The standard deviation of monthly, volume-weighted mean TEP concentration is highest in the Arctic region with approx. 50-150 µg C L^{-1}, while between 30°S-30°N, standard deviation is lowest with less than 5 µg C L^{-1} (Fig. 8B).

Engel et al. (2020) propose three different ocean regimes of TEP occurrence, to which we compare our model results: an oligotrophic regime, a polar regime, and an eastern boundary upwelling regime. The first, oligotrophic regime, is characterized by low phytoplankton productivity, which also results in low TEP concentrations. In large parts of the Atlantic, Pacific, and Indian Ocean, the modeled TEP concentration ranges between 5 and 25 µg C L^{-1} in the annual average, without a notable seasonal cycle. This agrees to *in situ* data: Data reviewed in Zamanillo et al., (2019) supports this pattern with a range of 5-36 µg C L^{-1}. Particularly, in the tropical Atlantic, the TEP concentration is low at approx. 5-10 µg C L^{-1} (Engel et al., 2020; Wurl & Cunliffe, 2017).

According to Engel et al. (2020), within the second regime represented by the polar regions, TEP accumulates in the upper ocean layer. The authors contribute this mainly to the occurrence of the phytoplankton *Phaeocystis* spp. and microbial degradation focusing primarily on proteinaceous compounds rather than on TEP. For the Arctic Ocean, we discussed simulated TEP above (Section 3.3). In the Southern Ocean during the blooming period between December and March, modeled TEP concentrations increase to up to approx. 150 µg C L^{-1}, agreeing well to observational studies reporting values of 0-39 µg C L^{-1}, with higher values of approximately 200 µg C L^{-1} in Bransfield Strait (Engel et al., 2020; Wurl & Cunliffe, 2017; Zamanillo et al., 2019).

As a third regime, the eastern boundary upwelling systems are described as highly productive regimes, which also results in high TEP production in hand with fast particle sinking because of ballasting (Engel et al., 2020). Engel et al. (2020) report TEP values of up to 85 µg C L^{-1} in the Mauritanian and 9 µg C L^{-1} in the Peruvian upwelling system. Higher TEP amounts of up to 1200 µg C L^{-1} are reported for the California Currents (Zamanillo et al., 2019). Our setup of FESOM-REcoM does not simulate these regions properly in terms of primary productivity, and as a consequence, lacks this TEP pattern of eastern upwelling regimes as well. Overall, our simulated global TEP patterns are in good agreement with observational studies and can serve as a first milestone of modeling TEP in a large-scale ocean biogeochemical model.

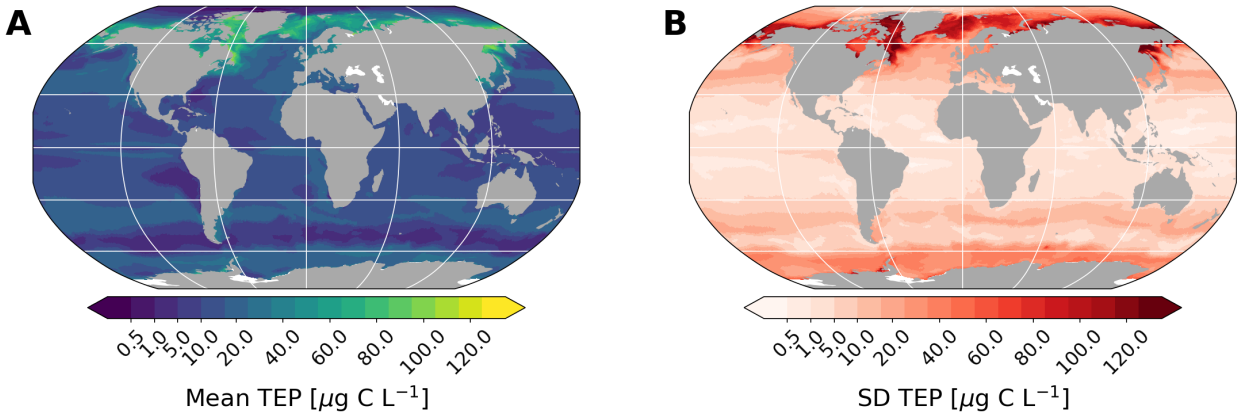

Figure 8. Maps of global TEP concentration as volume-weighted mean of 0-30 m of the years 2000-2019 (A) and its standard deviation (SD) (B).

4 Conclusions

The formation of organic carbon by phytoplankton plays a key role in the dynamics of marine ecosystems. Within this work, we have introduced for the first time parametrizations into a coupled ocean biogeochemical model to enable realistic predictions of production of dissolved carboxylic acid containing polysaccharides (PCHO) and Transparent Exopolymer Particles (TEP). The new setup proved good agreement to field and remote sensing measurements of phytoplankton biomass in terms of TChla. Although our implementation of PCHO formation as fraction of excreted organic carbon, the consecutive aggregation to TEP, and its remineralization, are very simplified assumptions, we could show that the use of this parametrization resulted in realistic simulations of spatial and seasonal dynamics of TEP concentration for the Arctic compared to *in situ* observations.

We focused in this study on PCHO and TEP distribution in the upper 30 m of the ocean column, as we are interested mainly in providing an understanding of biogenic aerosol precursors in the Arctic. With mean concentrations of 100-400 µg C L^{-1} in the upper 30 m of the ocean, TEP is available as a large pool of biogenic aerosol precursors. The particle itself can either be directly transported into the atmosphere or serve as a tracer in our simulation for the presence of other biogenic compounds which were not directly simulated in our model. Our results can also serve as a first baseline for a global assessment of biogenic aerosol precursors, as TEP concentration within FESOM-REcoM is in reasonable agreement with observations. Still, our setup is tuned for the Arctic realm specifically and another setup as e.g., Gürses et al. (2023) might be more adapted when broadening the research question to a global level.

Furthermore, with our over 30 years TEP simulations, diverging trends become visible. In the Fram Strait, Barents Sea and in the Eurasian Basin, TEP concentrations mostly decline over time, whereas there is an increase in the other parts of the Arctic Ocean, which is strongest in the Kara, Laptev and Beaufort Sea. We linked this change in the first case to a decrease in NPP, whereas in the second case, NPP increases with coinciding decrease of available nitrate concentration in the upper 30 m of the water column. This leads to stronger nutrient limitation of phytoplankton growth and results in the excretion of organic carbon according to the carbon overflow hypothesis (Engel et al. 2020). Even more in a warming ocean, the excretion of

polysaccharides has been suggested to increase (Engel et al., 2011), which could enhance the production of TEP as well.

Finally, this simulation can serve as an ocean component in Earth System Models to estimate the fluxes of biogenic aerosol precursors from the upper ocean into the atmosphere. TEP itself, but also other biogenic particles derived from the model output, can serve to better describe cloud formation and its microphysical properties in an atmospheric model. In this way, this study contributes to a better understanding of aerosol feedbacks in the Arctic realm.

Acknowledgments

We gratefully acknowledge the funding by the Deutsche Forschungsgemeinschaft (DFG, German Research Foundation) – Projektnummer 268020496 – TRR 172, within the Transregional Collaborative Research Center "ArctiC Amplification: Climate Relevant Atmospheric and SurfaCe Processes, and Feedback Mechanisms (AC)3 in subprojects B04, C03, D02. The contribution of SNL and AB was additionally funded by EU Horizon 2020 Coordination and Support Action (CSA) project KEPLER 2020-SPACE-2018-2020, grant agreement No. 821984 and further SNL contribution of SNL was partly made in the framework of the state assignment of the Federal Agency for Scientific Organizations (FASO) Russia (theme FMWE-2021-0014) before February 2022. Furthermore, the authors gratefully acknowledge the computing time granted by the Resource Allocation Board and provided on the supercomputer Lise and Emmy at NHR@ZIB and NHR@Göttingen as part of the NHR infrastructure. The calculations for this research were conducted with computing resources under the project hbk00084.

We thank O. Wurl and A. Engel and others for publishing valuable data on ocean surface concentration of various parameters, which helped to adjust and evaluate the model. We want to highlight multiple fruitful discussions within the PEBCAO team on this study.

We acknowledge the efforts of NASA, ESA, EUMETSAT, and CMEMS for the ocean color products.

740

741 ## Data availability

742 FESOM2.1-REcoM3 model source code is accessible at https://github.com/FESOM/fesom2. The
743 curated simulation results are available at https://doi.org/10.5281/zenodo.7886868 (Zeising et al.,
744 2023). The evaluation of model output was done using python3 (Python Software Foundation) and
745 the modules pyfesom2 (https://github.com/FESOM/pyfesom2) and py_f2recom (not published,
746 Maresys group, AWI), which are based on xarray, scipy, cartopy, and matplotlib, among others.
747 Observation data sets for model evaluation were obtained directly from the cited literature. The
748 Copernicus Marine Environment Monitoring Service level 4 monthly reprocessed Ocean Color
749 product (Product ID: OCEANCOLOUR_ARC_BGC_L4_MY_009_124) was obtained from
750 Copernicus Marine Data Store at
751 https://data.marine.copernicus.eu/product/OCEANCOLOUR_ARC_BGC_L4_MY_009_124/. The
752 Arctic Ocean TChla product presented in Lewis et al. (2020) was downloaded from Stanford Digital
753 Repository at https://doi.org/10.25740/kc822vj3040. The data set on DCCHO used in Jackowski et
754 al. (2020) is as well published at https://doi.pangaea.de/10.1594/PANGAEA.915751. The DCCHO
755 data set of the PASCAL campaign on RV Polarstern is available at PANGAEA (Zeppenfeld et al.,
756 2023). The Longhurst provinces were provided as shapefile by marineregions.org (Flanders Marine
757 Institute, 2009).

758

759 ## References

760 Alldredge, A. L., & Crocker, K. M. (1995). Why do sinking mucilage aggregates accumulate in
761 the water column? *Science of The Total Environment*, *165*(1), 15–22. doi:10.1016/0048-
762 9697(95)04539-D

763 Alldredge, A. L., Passow, U., & Logan, B. E. (1993). The abundance and significance of a class
764 of large, transparent organic particles in the ocean. *Deep Sea Research Part I: Oceanographic*
765 *Research Papers*, *40*(6), 1131–1140. doi:10.1016/0967-0637(93)90129-Q
766 Aller, J. Y., Radway, J. C., Kilthau, W. P., Bothe, D. W., Wilson, T. W., Vaillancourt, R. D., et
767 al. (2017). Size-resolved characterization of the polysaccharidic and proteinaceous components
768 of sea spray aerosol. *Atmospheric Environment*, *154*, 331–347.
769 doi:10.1016/j.atmosenv.2017.01.053
770 Álvarez, E., Thoms, S., Bracher, A., Liu, Y., & Völker, C. (2019). Modeling Photoprotection at
771 Global Scale: The Relative Role of Nonphotosynthetic Pigments, Physiological State, and
772 Species Composition. *Global Biogeochemical Cycles*, *33*. doi:10.1029/2018GB006101
773 von Appen, W.-J., Waite, A. M., Bergmann, M., Bienhold, C., Boebel, O., Bracher, A., et al.
774 (2021). Sea-ice derived meltwater stratification slows the biological carbon pump: results from
775 continuous observations. *Nature Communications*, *12*(1), 7309. doi:10.1038/s41467-021-26943-
776 z
777 Ardyna, M., & Arrigo, K. R. (2020). Phytoplankton dynamics in a changing Arctic Ocean.
778 *Nature Climate Change*, *10*(10), 892–903. doi:10.1038/s41558-020-0905-y
779 Arrigo, K. R., Perovich, D. K., Pickart, R. S., Brown, Z. W., van Dijken, G. L., Lowry, K. E., et
780 al. (2014). Phytoplankton blooms beneath the sea ice in the Chukchi Sea. *Deep Sea Research*
781 *Part II: Topical Studies in Oceanography*, *105*, 1–16.
782 Assmy, P., Fernández-Méndez, M., Duarte, P., Meyer, A., Randelhoff, A., Mundy, C. J., et al.
783 (2017). Leads in Arctic pack ice enable early phytoplankton blooms below snow-covered sea ice.
784 *Scientific Reports*, *7*, 40850.

785 Ayers, G. P., & Cainey, J. M. (2008). The CLAW hypothesis: a review of the major
786 developments. *Environmental Chemistry*, *4*(6), 366–374. doi:10.1071/EN07080
787 Azetsu-Scott, K., & Passow, U. (2004). Ascending marine particles: Significance of transparent
788 exopolymer particles (TEP) in the upper ocean. *Limnology and Oceanography*, *49*(3), 741–748.
789 doi:10.4319/lo.2004.49.3.0741
790 Bélanger, S., Babin, M., & Tremblay, J.-E. (2013). Increasing cloudiness in Arctic damps the
791 increase in phytoplankton primary production due to sea ice receding. *Biogeosciences*, *10*, 4087–
792 4101.
793 Block, K., Schneider, F. A., Mülmenstädt, J., Salzmann, M., & Quaas, J. (2020). Climate models
794 disagree on the sign of total radiative feedback in the Arctic. *Tellus A: Dynamic Meteorology*
795 *and Oceanography*, *72*(1), 1–14. doi:10.1080/16000870.2019.1696139
796 Charlson, R. J., Lovelock, J. E., Andreae, M. O., & Warren, S. G. (1987). Oceanic
797 phytoplankton, atmospheric sulphur, cloud albedo and climate. *Nature*, *326*(6114), 655–661.
798 doi:10.1038/326655a0
799 Cherkasheva, A., Bracher, A., Melsheimer, C., Köberle, C., Gerdes, R., Nöthig, E.-M., et al.
800 (2014). Influence of the physical environment on polar phytoplankton blooms: A case study in
801 the Fram Strait. *Journal of Marine Systems*, *132*, 196–207. doi:10.1016/j.jmarsys.2013.11.008
802 Copernicus Marine Service, & PML. (2022). Arctic Ocean Colour Plankton Multi-Year L4 daily
803 climatology and monthly observations [Data set]. Mercator Ocean International.
804 doi:10.48670/MOI-00293
805 Danilov, S., Sidorenko, D., Wang, Q., & Jung, T. (2017). The Finite-volumE Sea ice–Ocean
806 Model (FESOM2). *Geosci. Model Dev.*, *10*, 765–789. doi:10.5194/gmd-10-765-2017

807 Ebell, K., Nomokonova, T., Maturilli, M., & Ritter, C. (2020). Radiative Effect of Clouds at Ny-
808 Ålesund, Svalbard, as Inferred from Ground-Based Remote Sensing Observations. *Journal of*
809 *Applied Meteorology and Climatology*, *59*(1), 3–22. doi:10.1175/JAMC-D-19-0080.1
810 Engel, A. (2009). Determination of Marine Gel Particles. In *Practical Guidelines for the*
811 *Analysis of Seawater* (pp. 125–142). Boca Raton, USA: CRC-Press. Retrieved from
812 http://dx.doi.org/10.1201/9781420073072.ch7
813 Engel, A., Thoms, S., Riebesell, U., Rochelle-Newall, E., & Zondervan, I. (2004).
814 Polysaccharide aggregation as a potential sink of marine dissolved organic carbon. *Nature*,
815 *428*(6986), 929–932. doi:10.1038/nature02453
816 Engel, A., Händel, N., Wohlers, J., Lunau, M., Grossart, H.-P., Sommer, U., & Riebesell, U.
817 (2011). Effects of sea surface warming on the production and composition of dissolved organic
818 matter during phytoplankton blooms: results from a mesocosm study. *Journal of Plankton*
819 *Research*, *33*(3), 357–372. doi:10.1093/plankt/fbq122
820 Engel, A., Piontek, J., Metfies, K., Endres, S., Sprong, P., Peeken, I., et al. (2017). Inter-annual
821 variability of transparent exopolymer particles in the Arctic Ocean reveals high sensitivity to
822 ecosystem changes. *Scientific Reports*, *7*(1), 1–9.
823 Engel, A., Endres, S., Galgani, L., & Schartau, M. (2020). Marvelous Marine Microgels: On the
824 Distribution and Impact of Gel-Like Particles in the Oceanic Water-Column. *Frontiers in Marine*
825 *Science*, *7*, 405. doi:10.3389/fmars.2020.00405
826 Flanders Marine Institute. (2009). Longhurst Provinces. Retrieved from
827 https://www.marineregions.org/
828 Galgani, L., Piontek, J., & Engel, A. (2016). Biopolymers form a gelatinous microlayer at the
829 air-sea interface when Arctic sea ice melts. *Scientific Reports*, *6*, 29465. doi:10.1038/srep29465

Garcia, H., Weathers, K., Paver, C., Smolyar, I., Boyer, T., Locarnini, M., et al. (2019a). World ocean atlas 2018. Vol. 4: Dissolved inorganic nutrients (phosphate, nitrate and nitrate+ nitrite, silicate). *A. Mishonov Technical Editor, Tech. Rep.*, *NOAA Atlas NESDIS*(84).

Garcia, H., Weathers, K., Paver, C., Smolyar, I., Boyer, T., Locarnini, M., et al. (2019b). World Ocean Atlas 2018, Volume 3: Dissolved Oxygen, Apparent Oxygen Utilization, and Dissolved Oxygen Saturation. *A. Mishonov Technical Editor, Tech. Rep.*, *NOAA Atlas NESDIS*(83).

Goosse, H., Kay, J. E., Armour, K. C., Bodas-Salcedo, A., Chepfer, H., Docquier, D., et al. (2018). Quantifying climate feedbacks in polar regions. *Nature Communications*, *9*(1), 1919. doi:10.1038/s41467-018-04173-0

Gürses, Ö., Oziel, L., Karakus, O., Sidorenko, D., Völker, C., Ye, Y., et al. (2023). Ocean biogeochemistry in the coupled ocean-sea ice-biogeochemistry model FESOM2.1-REcoM3. *Geosci. Model Dev. Discuss.*, *2023*, 1–73. doi:10.5194/gmd-2023-2

Gürses, Özgür. (2021). FESOM2.1-REcoM2.1. *Geoscientific Model Development*.

Hartmann, M., Adachi, K., Eppers, O., Haas, C., Herber, A., Holzinger, R., et al. (2020). Wintertime Airborne Measurements of Ice Nucleating Particles in the High Arctic: A Hint to a Marine, Biogenic Source for Ice Nucleating Particles. *Geophysical Research Letters*, *47*(13), e2020GL087770. doi:10.1029/2020GL087770

Hauck, J., Völker, C., Wang, T., Hoppema, M., Losch, M., & Wolf-Gladrow, D. A. (2013). Seasonally different carbon flux changes in the Southern Ocean in response to the southern annular mode. *Global Biogeochemical Cycles*, *27*(4), 1236–1245. doi:10.1002/2013GB004600

Hauck, J., Zeising, M., Le Quéré, C., Gruber, N., Bakker, D. C. E., Bopp, L., et al. (2020). Consistency and Challenges in the Ocean Carbon Sink Estimate for the Global Carbon Budget. *Frontiers in Marine Science*, *7*, 571720. doi:10.3389/fmars.2020.571720

853 Hawkins, L. N., & Russell, L. M. (2010). Polysaccharides, Proteins, and Phytoplankton
854 Fragments: Four Chemically Distinct Types of Marine Primary Organic Aerosol Classified by
855 Single Particle Spectromicroscopy. *Advances in Meteorology*, *2010*, 612132-.
856 doi:10.1155/2010/612132
857 Heim, B., Abramova, E., Doerffer, R., Günther, F., Hölemann, J., Kraberg, A., et al. (2014).
858 Ocean colour remote sensing in the southern Laptev Sea: evaluation and applications.
859 *Biogeosciences*, *11*(15), 4191–4210. doi:10.5194/bg-11-4191-2014
860 Hunke, E., Allard, R., Bailey, D. A., Blain, P., Craig, A., Dupont, F., et al. (2020, March). CICE-
861 Consortium/Icepack: Icepack 1.2.1 (Version 1.2.1). Zenodo. doi:10.5281/zenodo.3712299
862 Ingvaldsen, R. B., Assmann, K. M., Primicerio, R., Fossheim, M., Polyakov, I. V., & Dolgov, A.
863 V. (2021). Physical manifestations and ecological implications of Arctic Atlantification. *Nature*
864 *Reviews Earth & Environment*, *2*(12), 874–889. doi:10.1038/s43017-021-00228-x
865 Intrieri, J. M. (2002). An annual cycle of Arctic surface cloud forcing at SHEBA. *Journal of*
866 *Geophysical Research*, *107*(C10), 8039. doi:10.1029/2000JC000439
867 Irish, V. E., Elizondo, P., Chen, J., Chou, C., Charette, J., Lizotte, M., et al. (2017). Ice-
868 nucleating particles in Canadian Arctic sea-surface microlayer and bulk seawater. *Atmospheric*
869 *Chemistry and Physics*, *17*(17), 10583–10595. doi:10.5194/acp-17-10583-2017
870 von Jackowski, A., Grosse, J., Nöthig, E.-M., & Engel, A. (2020). Dynamics of organic matter
871 and bacterial activity in the Fram Strait during summer and autumn. *Philosophical Transactions*
872 *of the Royal Society A: Mathematical, Physical and Engineering Sciences*, *378*(2181), 20190366.
873 doi:10.1098/rsta.2019.0366

874 Janout, M. A., Hölemann, J., Waite, A. M., Krumpen, T., von Appen, W.-J., & Martynov, F.
875 (2016). Sea-ice retreat controls timing of summer plankton blooms in the Eastern Arctic Ocean.
876 *Geophysical Research Letters*, *43*(24), 12,493-12,501. doi:10.1002/2016GL071232
877 Jung, J., Lee, Y., Cho, K.-H., Yang, E. J., & Kang, S.-H. (2022). Spatial Distributions of
878 Riverine and Marine Dissolved Organic Carbon in the Western Arctic Ocean: Results From the
879 2018 Korean Expedition. *Journal of Geophysical Research: Oceans*, *127*(7), e2021JC017718.
880 doi:10.1029/2021JC017718
881 Karakuş, O., Völker, C., Iversen, M., Hagen, W., Gladrow, D. W., Fach, B., & Hauck, J. (2021).
882 Modeling the Impact of Macrozooplankton on Carbon Export Production in the Southern Ocean.
883 *Journal of Geophysical Research: Oceans*, *n/a*(n/a), e2021JC017315.
884 doi:10.1029/2021JC017315
885 Koldunov, N. V., Aizinger, V., Rakowsky, N., Scholz, P., Sidorenko, D., Danilov, S., & Jung, T.
886 (2019). Scalability and some optimization of the Finite-volumE Sea ice–Ocean Model, Version
887 2.0 (FESOM2). *Geoscientific Model Development*, *12*(9), 3991–4012. doi:10.5194/gmd-12-
888 3991-2019
889 Krembs, C., & Deming, J. W. (2008). The role of exopolymers in microbial adaptation to sea ice.
890 In *Psychrophiles: from biodiversity to biotechnology* (pp. 247–264). Springer.
891 Kwok, R. (2018). Arctic sea ice thickness, volume, and multiyear ice coverage: losses and
892 coupled variability (1958–2018). *Environmental Research Letters*, *13*(10), 105005.
893 doi:10.1088/1748-9326/aae3ec
894 Lauvset, S. K., Key, R. M., Olsen, A., van Heuven, S., Velo, A., Lin, X., et al. (2016). A new
895 global interior ocean mapped climatology: the 1° × 1° GLODAP version 2. *Earth Syst. Sci.*
896 *Data*, *8*(2), 325–340. doi:10.5194/essd-8-325-2016

Leck, C., & Bigg, E. K. (2007). A modified aerosol - cloud - climate feedback hypothesis. *Environmental Chemistry*, *4*(6), 400.

Lewis, K. M., & Arrigo, K. R. (2020). Ocean Color Algorithms for Estimating Chlorophyll a, CDOM Absorption, and Particle Backscattering in the Arctic Ocean. *Journal of Geophysical Research: Oceans*, *125*(6), e2019JC015706. doi:10.1029/2019JC015706

Lewis, K. M., van Dijken, G. L., & Arrigo, K. R. (2020). Changes in phytoplankton concentration now drive increased Arctic Ocean primary production. *Science*, *369*(6500), 198–202. doi:10.1126/science.aay8380

Longhurst, A. R. (2006). *Ecological geography of the sea* (2nd Edition). San Diego: Academic Press.

Macke, A., & Flores, H. (2018, June). The expeditions PS106/1 and 2 of the research vessel POLARSTERN to the arctic ocean in 2017. Bremerhaven: Alfred Wegener Institute for Polar and Marine Research. doi:10.2312/BzPM_0719_2018

Nöthig, E.-M., Bracher, A., Engel, A., Metfies, K., Niehoff, B., Peeken, I., et al. (2015). Summertime plankton ecology in Fram Strait—a compilation of long- and short-term observations. *Polar Research*, *34*(1), 23349. doi:10.3402/polar.v34.23349

Nöthig, E.-M., Ramondenc, S., Haas, A., Hehemann, L., Walter, A., Bracher, A., et al. (2020). Summertime Chlorophyll a and Particulate Organic Carbon Standing Stocks in Surface Waters of the Fram Strait and the Arctic Ocean (1991–2015). *Frontiers in Marine Science*, *7*, 350. doi:10.3389/fmars.2020.00350

Ogawa, H., & Tanoue, E. (2003). Dissolved Organic Matter in Oceanic Waters. *Journal of Oceanography*, *59*(2), 129–147. doi:10.1023/A:1025528919771

Orellana, M. V., Matrai, P. A., Leck, C., Rauschenberg, C. D., Lee, A. M., & Coz, E. (2011). Marine microgels as a source of cloud condensation nuclei in the high Arctic. *Proc. Natl. Acad. Sci.*, *108*(33), 13612–13617. doi:10.1073/pnas.1102457108

Oziel, L., Schourup-Kristensen, V., Wekerle, C., & Hauck, J. (2022). The Pan-Arctic Continental Slope as an Intensifying Conveyer Belt for Nutrients in the Central Arctic Ocean (1985–2015). *Global Biogeochemical Cycles*, *36*(6), e2021GB007268. doi:10.1029/2021GB007268

Pakulski, J. D., & Benner, R. (1994). Abundance and distribution of carbohydrates in the ocean. *Limnology and Oceanography*, *39*(4), 930–940.

Park, J., Dall'Osto, M., Park, K., Kim, J.-H., Park, J., Park, K.-T., et al. (2019). Arctic Primary Aerosol Production Strongly Influenced by Riverine Organic Matter. *Environmental Science & Technology*, *53*(15), 8621–8630. doi:10.1021/acs.est.9b03399

Passow, U. (2002). Production of transparent exopolymer particles (TEP) by phyto- and bacterioplankton. *Mar Ecol Prog Ser*, *236*, 1–12.

Peralta-Ferriz, C., & Woodgate, R. A. (2015). Seasonal and interannual variability of pan-Arctic surface mixed layer properties from 1979 to 2012 from hydrographic data, and the dominance of stratification for multiyear mixed layer depth shoaling. *Progress in Oceanography*, *134*, 19–53. doi:10.1016/j.pocean.2014.12.005

van Pinxteren, M., Robinson, T.-B., Zeppenfeld, S., Gong, X., Bahlmann, E., Fomba, K. W., et al. (2022). High number concentrations of transparent exopolymer particles in ambient aerosol particles and cloud water – a case study at the tropical Atlantic Ocean. *Atmos. Chem. Phys.*, *22*(8), 5725–5742. doi:10.5194/acp-22-5725-2022

940 Piontek, J., Galgani, L., Nöthig, E.-M., Peeken, I., & Engel, A. (2021). Organic matter
941 composition and heterotrophic bacterial activity at declining summer sea ice in the central Arctic
942 Ocean. *Limnology and Oceanography*, *66*(S1), S343–S362. doi:10.1002/lno.11639
943 Pithan, F., & Mauritsen, T. (2014). Arctic amplification dominated by temperature feedbacks in
944 contemporary climate models. *Nature Geoscience*, *7*(3), 181–184. doi:10.1038/ngeo2071
945 Pörtner, H.-O., Roberts, D., Masson-Delmotte, V., Zhai, P., Tignor, M., Poloczanska, E., et al.
946 (2019). The ocean and cryosphere in a changing climate. A special report of the
947 intergovernmental panel on climate change. *Intergovernmental Panel on Climate Change*, 1–
948 765.
949 Randelhoff, A., Holding, J., Janout, M., Sejr, M. K., Babin, M., Tremblay, J.-É., & Alkire, M. B.
950 (2020). Pan-Arctic Ocean Primary Production Constrained by Turbulent Nitrate Fluxes.
951 *Frontiers in Marine Science*, *7*, 150. doi:10.3389/fmars.2020.00150
952 Rantanen, M., Karpechko, A. Yu., Lipponen, A., Nordling, K., Hyvärinen, O., Ruosteenoja, K.,
953 et al. (2022). The Arctic has warmed nearly four times faster than the globe since 1979.
954 *Communications Earth & Environment*, *3*(1), 168. doi:10.1038/s43247-022-00498-3
955 Robinson, T.-B., Stolle, C., & Wurl, O. (2019). Depth is relative: the importance of depth for
956 transparent exopolymer particles in the near-surface environment. *Ocean Science*, *15*(6), 1653–
957 1666.
958 Robinson, T.-B., Giebel, H.-A., & Wurl, O. (2019). Riding the Plumes: Characterizing Bubble
959 Scavenging Conditions for the Enrichment of the Sea-Surface Microlayer by Transparent
960 Exopolymer Particles. *Atmosphere*, *10*(8), 454. doi:10.3390/atmos10080454

961 Schartau, M., Engel, A., Schröter, J., Thoms, S., Völker, C., & Wolf-Gladrow, D. (2007).
962 Modelling carbon overconsumption and the formation of extracellular particulate organic carbon.
963 *Biogeosciences Discussions*, *4*(1), 13–67.
964 Schmale, J., Zieger, P., & Ekman, A. M. L. (2021). Aerosols in current and future Arctic climate.
965 *Nature Climate Change*, *11*(2), 95–105. doi:10.1038/s41558-020-00969-5
966 Scholz, P., Sidorenko, D., Gurses, O., Danilov, S., Koldunov, N., Wang, Q., et al. (2019).
967 Assessment of the Finite-volumE Sea ice-Ocean Model (FESOM2.0) – Part 1: Description of
968 selected key model elements and comparison to its predecessor version. *Geosci. Model Dev.*,
969 *12*(11), 4875–4899. doi:10.5194/gmd-12-4875-2019
970 Schourup-Kristensen, V., Sidorenko, D., Wolf-Gladrow, D. A., & Völker, C. (2014). A skill
971 assessment of the biogeochemical model REcoM2 coupled to the Finite Element Sea Ice–Ocean
972 Model (FESOM 1.3). *Geoscientific Model Development*, *7*(6), 2769–2802. doi:10.5194/gmd-7-
973 2769-2014
974 Schourup-Kristensen, V., Wekerle, C., Wolf-Gladrow, D. A., & Völker, C. (2018). Arctic Ocean
975 biogeochemistry in the high resolution FESOM 1.4-REcoM2 model. *Progress in Oceanography*,
976 *168*, 65–81. doi:10.1016/j.pocean.2018.09.006
977 Schourup-Kristensen, V., Wekerle, C., Danilov, S., & Völker, C. (2021). Seasonality of
978 Mesoscale Phytoplankton Control in Eastern Fram Strait. *Journal of Geophysical Research:*
979 *Oceans*, *126*(10), e2021JC017279. doi:10.1029/2021JC017279
980 Serreze, M. C., & Barry, R. G. (2014). *The Arctic Climate System* (2nd ed.). Cambridge
981 University Press. doi:10.1017/CBO9781139583817

Serreze, M. C., & Meier, W. N. (2019). The Arctic's sea ice cover: trends, variability, predictability, and comparisons to the Antarctic. *Annals of the New York Academy of Sciences*, *1436*(1), 36–53. doi:10.1111/nyas.13856

Shupe, M. D., & Intrieri, J. M. (2004). Cloud Radiative Forcing of the Arctic Surface: The Influence of Cloud Properties, Surface Albedo, and Solar Zenith Angle. *Journal of Climate*, *17*(3), 616–628. doi:10.1175/1520-0442(2004)017<0616:CRFOTA>2.0.CO;2

Steele, D. J., Franklin, D. J., & Underwood, G. J. C. (2014). Protection of cells from salinity stress by extracellular polymeric substances in diatom biofilms. *Biofouling*, *30*(8), 987–998. doi:10.1080/08927014.2014.960859

Steele, M., Morley, R., & Ermold, W. (2001). PHC: A Global Ocean Hydrography with a High-Quality Arctic Ocean. *Journal of Climate*, *14*(9), 2079–2087. doi:10.1175/1520-0442(2001)014<2079:PAGOHW>2.0.CO;2

Stroeve, J., & Notz, D. (2018). Changing state of Arctic sea ice across all seasons. *Environmental Research Letters*, *13*(10), 103001.

Taylor, P. C., Boeke, R. C., Boisvert, L. N., Feldl, N., Henry, M., Huang, Y., et al. (2022). Process Drivers, Inter-Model Spread, and the Path Forward: A Review of Amplified Arctic Warming. *Frontiers in Earth Science*, *9*. Retrieved from https://www.frontiersin.org/article/10.3389/feart.2021.758361

Terhaar, J., Lauerwald, R., Regnier, P., Gruber, N., & Bopp, L. (2021). Around one third of current Arctic Ocean primary production sustained by rivers and coastal erosion. *Nature Communications*, *12*(1), 169. doi:10.1038/s41467-020-20470-z

1003 Tsujino, H., Urakawa, S., Nakano, H., Small, R. J., Kim, W. M., Yeager, S. G., et al. (2018).
1004 JRA-55 based surface dataset for driving ocean–sea-ice models (JRA55-do). *Ocean Modelling*,
1005 *130*, 79–139. doi:10.1016/j.ocemod.2018.07.002
1006 Vihma, T., Screen, J., Tjernström, M., Newton, B., Zhang, X., Popova, V., et al. (2016). The
1007 atmospheric role in the Arctic water cycle: A review on processes, past and future changes, and
1008 their impacts. *Journal of Geophysical Research: Biogeosciences*, *121*(3), 586–620.
1009 doi:10.1002/2015JG003132
1010 Wang, Q., Danilov, S., Sidorenko, D., Timmermann, R., Wekerle, C., Wang, X., et al. (2014).
1011 The Finite Element Sea Ice-Ocean Model (FESOM) v.1.4: formulation of an ocean general
1012 circulation model. *Geoscientific Model Development*, *7*(2), 663–693. doi:10.5194/gmd-7-663-
1013 2014
1014 Wang, Q., Wekerle, C., Danilov, S., Wang, X., & Jung, T. (2018). A 4.5 km resolution Arctic
1015 Ocean simulation with the global multi-resolution model FESOM 1.4. *Geoscientific Model*
1016 *Development*, *11*(4), 1229–1255. doi:10.5194/gmd-11-1229-2018
1017 Wang, Qiang, Koldunov, N. V., Danilov, S., Sidorenko, D., Wekerle, C., Scholz, P., et al.
1018 (2020). Eddy Kinetic Energy in the Arctic Ocean From a Global Simulation With a 1-km Arctic.
1019 *Geophysical Research Letters*, *47*(14), e2020GL088550. doi:10.1029/2020GL088550
1020 Wekerle, C., Wang, Q., Danilov, S., Schourup-Kristensen, V., von Appen, W.-J., & Jung, T.
1021 (2017). Atlantic Water in the Nordic Seas: Locally eddy-permitting ocean simulation in a global
1022 setup. *Journal of Geophysical Research: Oceans*, *122*(2), 914–940. doi:10.1002/2016JC012121
1023 Wendisch, M., Macke, A., Ehrlich, A., Lüpkes, C., Mech, M., Chechin, D., et al. (2019). The
1024 Arctic cloud puzzle: Using ACLOUD/PASCAL multiplatform observations to unravel the role

of clouds and aerosol particles in arctic amplification. *Bulletin of the American Meteorological Society*, *100*(5), 841–871.

Wilson, T. W., Ladino, L. A., Alpert, P. A., Breckels, M. N., Brooks, I. M., Browse, J., et al. (2015). A marine biogenic source of atmospheric ice-nucleating particles. *Nature*, *525*(7568), 234–238. doi:10.1038/nature14986

Wurl, O., Wurl, E., Miller, L., Johnson, K., & Vagle, S. (2011). Formation and global distribution of sea-surface microlayers. *Biogeosciences*, *8*(1), 121–135. doi:10.5194/bg-8-121-2011

Wurl, Oliver, & Cunliffe, M. (2017). Transparent exopolymeric particles: an important EPS component in seawater. *The Perfect Slime: Microbial Extracellular Polymeric Substances (EPS)*, 249.

Yamada, Y., Fukuda, H., Uchimiya, M., Motegi, C., Nishino, S., Kikuchi, T., & Nagata, T. (2015). Localized accumulation and a shelf-basin gradient of particles in the Chukchi Sea and Canada Basin, western Arctic. *Journal of Geophysical Research: Oceans*, *120*(7), 4638–4653. doi:10.1002/2015JC010794

Zamanillo, M., Ortega-Retuerta, E., Nunes, S., Rodríguez-Ros, P., Dall'Osto, M., Estrada, M., et al. (2019). Main drivers of transparent exopolymer particle distribution across the surface Atlantic Ocean. *Biogeosciences*, *16*(3), 733–749. doi:10.5194/bg-16-733-2019

Zampieri, L., Kauker, F., Fröhle, J., Sumata, H., Hunke, E. C., & Goessling, H. F. (2021). Impact of Sea-Ice Model Complexity on the Performance of an Unstructured-Mesh Sea-Ice/Ocean Model under Different Atmospheric Forcings. *Journal of Advances in Modeling Earth Systems*, *13*(5), e2020MS002438. doi:10.1029/2020MS002438

1047 Zeising, M., Oziel, L., Gürses, Ö., Hauck, J., Losa, S., Thoms, S., & Bracher, A. (2023).
1048 FESOM2.1-REcoM3 4.5 km model analysis for biogenic aerosol precursors in the Arctic Ocean.
1049 *Zenodo*. Retrieved from https://doi.org/10.5281/zenodo.7886868
1050 Zeppenfeld, S., Bracher, A., Wiegmann, S., Zeising, M., Fuchs, S., Van Pinxteren, M., &
1051 Herrmann, H. (2023). Dissolved and particulate combined carbohydrates, pH, inorganic ions,
1052 CDOM and particulate absorption of SML and bulk water in Arctic surface seawater and melt
1053 ponds. *PANGAEA - Data Publisher for Earth & Environmental Science*. Retrieved from
1054 https://doi.org/xx.xx/PANGAEA.xxxxxx [DOI registration in progess]
1055 Zeppenfeld, S., van Pinxteren, M., Engel, A., & Herrmann, H. (2020). A protocol for quantifying
1056 mono- and polysaccharides in seawater and related saline matrices by electro-dialysis (ED) –
1057 combined with HPAEC-PAD. *Ocean Science*, *16*(4), 817–830. doi:10.5194/os-16-817-2020
1058 Zeppenfeld, Sebastian, van Pinxteren, M., Hartmann, M., Bracher, A., Stratmann, F., &
1059 Herrmann, H. (2019). Glucose as a Potential Chemical Marker for Ice Nucleating Activity in
1060 Arctic Seawater and Melt Pond Samples. *Environmental Science & Technology*, *53*(15), 8747–
1061 8756. doi:10.1021/acs.est.9b01469